Intravital multi-modal flux analysis reveals the transport mechanism of bile acids through hepatic microconduits

Authors: Nachiket Vartak[1*], Georgia Guenther[1#], Florian Joly[2#], Amruta Damle-Vartak[1], Gudrun Wibbelt[8], Jörns Fickel[8,10], Simone Jörs[4], Brigitte Begher-Tibbe[1], Adrian Friebel[3], Kasimir Wansing[3], Ahmed Ghallab[1,7], Marie Rosselin[5], Noemie Boissier[2], Irene Vignon-Clementel[2], Christian Hedberg[5], Fabian Geisler[4], Heribert Hofer[8,9], Peter Jansen[6], Stefan Hoehme[3], Dirk Drasdo[2,1], Jan G. Hengstler[1*]

Affiliations:

[1] Leibniz Research Centre for Working Environment and Human Factors (IfADo), Dortmund, Germany

[2] Inria, Paris, France

[3] Institute for Computer Science, Leipzig, Germany

[4] Klinikum rechts der Isar, Technical University Munich, Munich, Germany

[5] Umeå University, Umeå, Sweden

[6] Universiteit van Amsterdam, Amsterdam, Netherlands

[7] Faculty of Veterinary Medicine, South Valley University, Qena, Egypt.

[8] Leibniz Institute for Zoo and Wildlife Research (IWZ), Berlin, Germany

[9] Freie Universität Berlin, Berlin, Germany

[10] University of Potsdam, Potsdam-Golm, Germany

# These authors contributed equally to the manuscript.

*Correspondence to: Nachiket Vartak, Email: vartak@bioimaging.tech

Jan G. Hengstler, Email: hengstler@ifado.de

Abstract (max 125 words):

Small-molecule flux in tissue-microdomains is essential for organ function, but knowledge of this process is scant due to the lack of suitable methods applicable to live animals. We developed a methodology based on dynamic and correlative imaging for quantitative intravital flux analysis. Application to the liver, challenged the prevailing 'mechano-osmotic' theory of canalicular bile flow. After active transport across hepatocyte membranes bile salts are transported in the canaliculi primarily by diffusion. Only in the interlobular ducts, diffusion is augmented by regulatable advection. We corroborate these observations with in silico simulations and pan-species comparisons of lobule size. This study demonstrates a flux mechanism, where the energy invested in transmembrane transport entropically dissipates in a sub-micron scale vessel network.

One Sentence Summary (max 40 char):

Bile flux proceeds by diffusion in canaliculi, augmented by advection in ducts.

Main Text:

The flux of small molecules through tissue compartments and vessel networks is a fundamental process supporting organ function. Analysis of flux in microscopic vessels, cells and tissue compartments in living organisms remains intractable due to their inaccessibility to conventional rheological and ultrasonic methods. In this work, we used the liver as an exemplary organ and quantified transport in its microscopic biliary conduits. Liver tissue architecture consists of lobules — functional units comprised of blood capillaries called sinusoids, hepatocytes, and a canalicular network formed by hepatocyte apical membranes (Fig 1A). The canalicular networks are linked to interlobular bile ducts (IBDs), which progressively converge into larger ducts and finally the extrahepatic bile duct (EHBD) (*1*).

Prevailing thought ascribes the movement of bile and its constituent small molecules (bile acids, xenobiotics etc.) to fluid advection due to osmotic water influx and canalicular membrane contractility (*2*). Hepatocyte-mediated active transport of bile acids and other organic solutes into the canalicular lumen is expected to generate an osmotic gradient that drives the movement of water and causes flow of canalicular bile. Bile would then be pushed through the network with an increasing velocity towards IBDs, supported by peristalsis-like contractions of canalicular membranes (*3*). However, this 'mechano-osmotic bile flow' hypothesis is only an intuitive interpretation from macro-scale observations of the amount of biliary fluid and concentration of bile acids exiting the EHBD, and of mathematical modeling. We established Intravital Arbitrary Region Image Correlation Spectroscopy (*IVA*RICS), fluorescence loss after photoactivation (FLAP) and time-lapse microscopy techniques to quantify flux in microdomains in live organisms and elucidated the mode of biliary flux.

Results

Intravital analysis of bile flux was enabled by HNF1beta/CreER-reporter mice which express tdTomato in cholangiocytes, and through the use of fluorescent analogs of bile salts.

Fluorescent analogs such as cholyl-lysyl fluorescein (CLF) are transported by hepatocytes from sinusoids to canaliculi, allowing direct visualization of the canalicular network. Confocal or 2-photon imaging of live mouse livers show the canalicular networks and connecting interlobular bile ducts, depicting the basic lobular architecture in which biliary flux occurs (Fig. 1A).

Determination of local flux mechanisms and the bounds of flux kinetics in the liver canalicular network

Bile flux may occur either by advection or by inherent diffusion of the bile salts through the canalicular space, or a combination of both (convection). To investigate the local flux mechanisms, we utilized fluorescence loss after photo-activation (FLAP) of a photoactivatable analog of fluorescein (CMNB-Fluorescein) in intravital microscopy of mouse livers. Following tail vein injection, CMNB-Fluorescein was photo-activated at time points when it was almost entirely localized in the canalicular network. Repeated photoactivation of CMNB-Fluorescein was performed in a pulsed manner on predefined regions of known spatial dimensions (Fig. 1B). By varying time-intervals between the photoactivation pulses, a race-condition is set up in the defined region between photoactivation pulses which increase fluorescence, and the underlying flux mechanism which depletes fluorescence. Accumulation of fluorescence with subsequent pulses indicates insufficiency of the underlying flux to remove the fluorescent material in the time interval between pulses. By decreasing the activation pulse rate until the underlying flux rate could finally remove the fluorescent material in the time-interval between, an upper-bound of the flux rate was established. Assuming pure advection in the canaliculi, the upper limit of the flux rate was determined to be **~0.05 µm/s** as the ratio of the maximum length activated region and the minimum interval between pulses in which it is depleted. Correspondingly, assuming pure diffusion, a lower bound of **0.5 µm²/s** is obtained for the diffusion coefficient from the ratio of the area of the activated region and the time interval required to deplete fluorescence in the region. These limits of the flux rates of advection or diffusion suggest that the inherent diffusion of small molecule solutes such as bile acids dominates their transport, rather than advection of the solvent.

FLAP differentiates the diffusion-dominated and advection-augmented compartments of the biliary system

To determine the mechanism of bile flux, we examined the nature of the fluorescence loss in the photoactivated (FLAP) region after a single photoactivation pulse in the canalicular network. At initial timepoints, the loss of fluorescence in the circular activated region is symmetric with a corresponding symmetric spread outside this region, irrespective of the lobular location of the activated zone (Fig 1C, Mov. S1). The location of the fluorescence maximum within the activated zone remains invariant over time. Alternative activation geometries (stripe) led to identical conclusions (Fig. S1A, Mov. S2). This indicates that the local biliary flux in canaliculi is **not vectorial** but rather, the dispersion of bile salts is symmetric and omnidirectional in the canalicular network. This implies molecular diffusion rather than vectorial flow as the primary flux mechanism in the canalicular network, consistent with the extremely low upper bound of pure advection in the canalicular network. The same intravital photoactivation technique was applied to intralobular bile ducts (Fig. 1C) that were specifically visualized through the cholangiocyte-specific tdTomato-fluorescence-labeling in the HNF1beta/CreER-tdTomato mice. Contrary to observations in canaliculi, dispersion of fluorescence was asymmetrical with vectorial bias along one direction in the IBD. This indicates the presence of advection, in addition to diffusion, that underlies bile flux in the interlobular ducts.

To directly visualize diffusion-dominance in the canalicular network, we performed FLAP experiments at the Canal of Hering (CoH) - connections of the canalicular network to IBDs. These junctional regions represent the transition zone from a diffusion-dominated canalicular lumen to an advection-augmented ductular lumen. Photoactivated CMNB-Fluorescein in the canalicular network adjacent to the CoH (i.e. PV zone) transited to the IBD and diffused symmetrically into the network as expected (Fig. 1D). However, photoactivated CMNB-Fluorescein in the CoH also transited retrograde into the canalicular network. This retrograde flux of fluorescence from the CoH into the canalicular network confirmed that in the canalicular network, the inherent diffusion of small molecules overrules the meagre (if any) advection towards the bile duct.

The insignificant canalicular advection under basal conditions led us to test if conventional interventions that are known to increase extrahepatic bile flow could induce canalicular advection. Secretin is known to stimulate bile flow from the bile duct epithelium (*4*) and is expected to increase extrahepatic bile flow without increasing canalicular flux. In contrast, taurocholate (TCA) is excreted into canaliculi and expected to cause hyperosmotic water influx (*5*) to increase canalicular bile flow. Secretin as well as TCA infusion both induced an increase in extrahepatic bile flow (Fig 2A) confirming previous reports.

Photoactivation in various lobular zones and interlobular bile ducts was performed (Fig. 2B, Mov. S3) and the half-life of clearance was determined (Fig. S1B). Relative contributions of diffusion and advection were determined by quantification of the dispersion and displacement of Gaussian photo-activation profiles for the diffusion coefficient and velocity, respectively (*6*) (Supplementary information).

Under basal conditions, diffusion was similar in the interlobular ducts and all lobular zones of the canalicular network, ranging between median diffusion coefficients of **2-5 μm^2/s** (Fig. 2C, Table S1). However, the advective velocity in canalicular networks was **less than 0.02 μm/s**. In contrast, bile ducts showed an advective velocity ranging from **1-1.2 μm/s**. These findings reinforce the finding that biliary flux is diffusion-dominated in the canalicular network but show that it is augmented by advection in the bile ducts. Following secretin administration or TCA infusion, advection in the canalicular network did not significantly increase and the diffusion coefficient remained similar to that under basal conditions. In the interlobular bile ducts, the diffusion coefficient also remained unchanged from that of basal conditions, but the median advection velocity increased to up to **3.8 μm/s after secretin administration** and up to **6.2 μm/s during TCA-infusion** (Fig. 2C, Table S1). These findings are consistent with the known property of cholangiocytes to secrete water upon secretin stimulation (*7*) or when excess bile salts are detected in the bloodstream (*8*). Yet, even under these conditions, we find that the canalicular bile flux remains diffusion-dominated.

Quantification of flux parameters for diffusion and advection Intravital <u>A</u>rbitrary <u>R</u>egion <u>I</u>mage <u>C</u>orrelation <u>S</u>pectroscopy (IVARICS)

The lack of any substantial flow in the canalicular network contradicts popular conjecture, and the quantification methods used (*6*) assume a homogeneous fluid medium without diffusion barriers. Non-ideal conditions in a living mouse such as inherent inhomogeneity of the canalicular network, its finite size, boundary at the central vein and the sink at the CoH/IBD may affect the photo-activation profiles. To remove the effect of these non-ideal morphological constraints on determination of flux parameters, we established an orthogonal approach to determine diffusion and advection rates in the biliary compartments – namely, Intravital Arbitrary Region Image Correlation Spectroscopy (*IVA*RICS). Image correlation spectroscopies (ICS) (*9, 10*) are based on rapid local acquisition of fluorescence fluctuation in a defined region and the generation of corresponding correlation maps. The method is intrinsically local and yields apparent diffusion coefficients for the acquisition region. We first determined the feasibility of applying image correlation methods in vivo, by acquiring conventional spatial and temporal ICS sequences in the liver sinusoids, hepatocytes and canaliculi of mice infused with CLF. Since sinusoidal blood flow comprises diffusion and advection, while the hepatocyte cytoplasm comprises only diffusion, these compartments served as *in situ* controls. IVARICS sequences could be used to extract the flux mechanism – sinusoidal blood flow was measured to be ~60 µm/s and diffusion coefficients were ~2 µm^2/s in all compartments (Fig. 3A). No advection was detected in the hepatocyte cytoplasm as well as the canalicular lumen. The effect of animal movements due to heartbeat, respiration and intestinal peristalsis (Mov. S5) could be mitigated during post-processing using pruning of slow autocorrelations and the use of the recently reported arbitrary region raster ICS (RICS) algorithm (*11*) (Fig. 3B, see Supplementary Information). Spatial and temporal image correlation (RICS/TICS) was additionally used to fit the autocorrelation functions and determine diffusion coefficients and velocities (Fig. 3C,D, S2, Table S2, S3).

Diffusion coefficients and velocities derived from *IVARICS* analysis of CLF or fluorescein-infused mice confirmed the findings of the FLAP experiments (Fig. 2C, D, E). Median ductular advection velocity was measured to be ~1 µm/s under basal conditions, which increased upto a value of 2.4 µm/s by the action of secretin on the duct, and upto 3.7 µm/s through TCA infusion (Fig. 3E). Flow in the canalicular network remained negligible and was neither affected by secretin administration, nor by TCA infusion. Diffusion coefficients in the canalicular network and interlobular ducts ranged between 2.4-6 µm^2/s.

Image correlation techniques have distinct limitations from those of FLAP. They require a priori knowledge of the range in which flux parameters are expected, on which basis, image acquisition and fitting parameters have to be set. In the case of in vivo imaging, light scattering by tissue and movements of the animal during image acquisition (Fig. S2) must be compensated for during analysis (see Supplementary Information: IVARICS). Nevertheless, the general conclusion of the FLAP experiments was validated by *IVARICS*.

Simulation of Bile Flux in the liver

To validate if a system with diffusion-dominated canalicular flux, augmented by advection in the duct, is capable of accurately describing the behavior of bile acids in liver canalicular networks and ducts, we developed a deterministic Navier-Stokes *in silico model* in realistic canalicular geometries of the liver tissue. Confocal scans of immunofluorescence stained liver tissue showing canalicular network and interlobular bile ducts were generated as described previously (*12*) and digitized into triangulated meshes that served as the simulation space (Fig. 4A). Concentrations of fluorescein or CLF generated within various liver compartments during our experiments were estimated by establishing instrument calibration curves in murine bile in vitro (Fig. S3A). These concentrations, and the diffusion coefficients as well as velocities for the canalicular network and IBDs determined thus far were used as input parameters for the simulations.

The simulations accurately reproduced the behavior of small molecules in the canalicular network and IBDs. Simulations of repeated activation as described earlier (Fig. 1B) quantitatively reproduced the upper-bound of flux rates (Fig. 4B). Simulations of single photoactivations in the canalicular network reproduced symmetric canalicular dispersion and unidirectional displacement of intensity in the IBD (Fig. 4C) as was observed experimentally (Fig. 1C). The retrograde flux of fluorescence into the canalicular network from the CoH (Fig. 1D) was also accurately predicted by the simulations (Fig. 4D). The half-times of depletion in silico for a given area were similar to those observed in vivo (Fig. 4C, Fig. S1B), and varied proportionately to the area of photoactivation. In summary, the 'first-principles' simulation accurately described all experimental observations using experimentally derived

input parameters, reinforcing our findings of a diffusion-dominated canalicular network with negligible (if any) advection and an advection-augmented ductular system.

Factors (not) influencing global canalicular clearance rates

Water influx due to the osmotic gradient created by bile salts, wherein the cholic acid moiety represents the osmotically-active moiety, is the presumed *raison d'etre* for canalicular advection. Since our results so far indicate no such advection in the canalicular network, we addressed the effect of osmosis on global clearance of the bile salt analog cholyl-lysyl-fluorescein (CLF) from the liver lobule under basal or stimulated extrahepatic bile flow (TCA infusion, secretin administration) conditions. In particular, the effect of TCA to increase extrahepatic bile flow is ascribed to increased canalicular flow due to the aforementioned osmotic gradient (*2*).

Following an intravenous injection of CLF into the tail-vein, intravital time-lapse microscopy showed that the rate of CLF clearance from the canalicular network was unchanged between basal conditions or secretin- and TCA-stimulated conditions (Fig. 5A, B, D, Mov. S6). To rule out the possibility that the CLF molecule itself created a strong, perhaps maximal, osmotic gradient, we performed calibrated quantitative comparison of canalicular excretion of its fluorophore (fluorescein) with and without co-injection of its osmotically active component, cholic acid (*13*). Co-injection of cholic acid along with fluorescein did not significantly alter the kinetics of fluorescein excretion from the canalicular network (Fig. 5C, D, Mov. S7). These observations are not compatible with a role of osmosis in canalicular excretion. Co-injection of spectrally-distinct modified fluorescent bile acids with different hepatocyte export rates showed that canalicular excretion could not be saturated, and canalicular intensity remained correlated to the intensity in the hepatocytes (Fig. S3C, Table S4). Taken together, these results show that for bile acid concentrations of up to 400 µM (calibration curve, Fig. S3A) osmosis does not determine canalicular clearance rates of small molecules. Instead, differences in the hepatocyte transporter specificity/activity for fluorescein and CLF (*14, 15*) are likely to be the primary determinants of their clearance rates in liver tissue.

Evolutionary restriction of lobule size corroborates diffusion-dominated biliary flux

The time required for diffusive flux increases quadratically with the distance to be covered (*16*), and requires generation of higher canalicular concentrations of bile constituents to compensate for larger canalicular networks, to maintain the same clearance rate. Diffusion is thus an ineffective transport mechanism over large distances, imposing some sort of evolutionary spatial constraint (*17, 18*) over diffusion-reliant biological processes. We hypothesized that since the concentration of bile constituents that hepatocytes can generate in the canalicular network is restricted by the activity of their largely conserved molecular transporters (*19*), diffusion in the canalicular network imposes spatial limits on the size of the liver lobule if efficient clearance of bile constituents must be guaranteed.

To test this hypothesis, liver tissue of 24 mammalian species was immunostained for glutamine synthetase (GS) which is expressed in hepatocytes around the central vein and therefore indicates the center of liver lobules. Using a recently established automated image analysis procedure (*20*), the area of individual liver lobules was determined (Fig. 6A) for 24 species ranging from 21 g (mouse) to 4,500 kg (African elephant) in terms of body weight. Body weight and liver weight were strongly correlated across species with liver weight typically comprising ~2% of body weight. 6B, C, Table S5). Nuclear diameter of hepatocytes and nuclear density should not depend on body size, both were analyzed as negative controls (Fig. 6B, D), showing the expected lack of significant correlation with body weight. Lobule area correlated positively with body weight (Fig. 6B, C). However, while body weight and liver weight increased over more than five orders of magnitude, median lobule area increased only by ~1 order of magnitude from the smallest to the largest species (Fig. 6C). These results support the hypothesis that the size of canalicular networks, thus the lobular diameters must abide upper limits by diffusion.

Discussion and Conclusion

In this work, we combined advanced intravital imaging with simulation techniques in real geometries to investigate the flux characteristics of tissue microdomains. IVARICS is an adaptation of image correlation spectroscopy, where in the decay in correlation between pixels due to fluctuation of the signal created by molecular flux is used to compute the rate of

flux, with specialized corrections for periodic animal movements caused by its heartbeat, respiration and peristalsis. This allowed us to quantitatively decipher the mode of transport and determine its rate for small molecules in a sub-micron scale vessel network of arbitrary geometry. Utilizing FLAP studies, correlative imaging, immunostaining, rheological measurements and custom chemical probes, we have addressed a specific long-standing problem in liver physiology.

Our results show that, contrary to prevailing thought, bile acids are transported primarily through diffusion in the canaliculi, while being augmented by directional advection in the interlobular ducts. Through these observations, we deduced the compartmentalization of the liver into a diffusion-dominated canalicular domain where hepatocytes actively secrete small molecules and generate a concentration gradient that drives diffusive flux towards the IBDs (Fig. 6E). In IBDs, regulated and inducible water influx creates unidirectional advection which augments the diffusive flux. This induction can be caused either directly by hormones such as secretin (*21*), or indirectly by bile salts themselves as demonstrated for TCA (*22*), explaining the corresponding increase in extra-hepatic bile flow. This inducible increase in advection is restricted to the bile ducts, while the canalicular network remains nothing more than a standing-water zone.

This is in contradiction to the plausible, but as demonstrated here — apparently fallacious interpretation of a 'mechano-osmotic bile flow'. In hindsight, the secretion of bile acids by hepatocytes will necessitate simultaneous uptake of an anion such as Cl^- to maintain plasma membrane potential (*23*). Such a countercurrent anion uptake would likely counteract the development of any net osmotic pressure in the canalicular lumen. Direct studies on the osmotic effect of bile salts in bile secretion have only highlighted the importance of inorganic anions in ductular secretion (*24*), rather than bile salts in hepatocytes, consistent with our findings. Moreover, bile acids, as hydrophobic molecules, are incorporated in phospholipid micelles, preventing them from exerting their full osmotic potential. On the other hand, recent work shows that canaliculi contract autonomously and asynchronously at a low frequency of 6 events/hour through a calcium-dependent mechanism (*25*). This has been proposed to cause propulsion of bile in the canaliculi. However, the present analyses show that advection in the canaliculi does not exceed 0.02 μm/s, indicating that in the absence of *synchronized*

contractions along the CV-PV axis, merely mixing, rather than pumping of canalicular contents occurs.

One of the surprising aspects of flux in the canalicular network is the low diffusion coefficient of $2.4 - 4.6$ $\mu m^2/s$ (CI: 95%), compared to ~200 $\mu m^2/s$ in water in vitro (Fig. S3B). Biliary constituents such as albumin and phospholipid micelles may interact with bile acids to reduce their diffusivity. The apparent value of a diffusion coefficient may in fact represent the convolved diffusivity and binding interactions of multiple populations ranging from micellar to freely diffusion bile acid molecules. Nonetheless, the relatively low apparent diffusion coefficient is sufficient to explain local canalicular clearance rates, as verified by the diffusion simulation in realistic canalicular geometries. Rather, we show that hepatocyte cytoplasmic concentration is the strongest predictor of canalicular concentrations for bile salt analogs over the entire clearance period (Fig. S3C). Energy-dependent export from hepatocytes to the canalicular lumen is a more stringent bottleneck for bile acid clearance than the diffusive flux through the canalicular network.

A system lacking advection also lacks the ability to flush out precipitates and particulates, making it more susceptible to the consequences of exceeding the solubility limits of its constituents. Thus, the liver must maintain a fine balance between the generation of higher concentrations of bile acids to accelerate their excretion, while never surpassing their precipitation threshold. Failure to maintain this balance will result in precipitation of bile salts and blockage of the biliary conduits. The liver secretes amphipathic molecules such as phospholipids in bile to support solubilization, whose importance is underscored by the observation of bile crystals in Mdr2-deficient mice that cannot secrete phosphatidylcholine (*26*). These slow-diffusing bile crystals and precipitates lead to pathological consequences (*27, 28*) in the liver, and are a conspicuous feature in human diseases such as porphyria and Progressive familial intrahepatic cholestasis (PFIC).

Circumstantial evidence that efficient diffusion-dominated excretion in canaliculi imposes certain constraints on the size of the canalicular network is provided by the pan-species analysis of liver tissue. Liver weight scales with a constant ratio to body weight over 5 orders of magnitude while the lobule size only increases by ~1 order of magnitude. Evolutionarily, the liver may become as large as necessary, but lobular functional units of the liver are size-restricted.

This view of the liver, with a diffusion-dominated standing-water domain connected to an inducible flow-augmented excretion duct is a general principle applicable to exocrine glands (Fig. 6E, F). All exocrine glands contain an acinus, surrounded by epithelial cells that secrete their products into the acinar lumen. The lumen represents a reservoir where products accumulate to high concentrations, which is connected to an excretion duct in which flow can be induced on demand. A similar design enables the function of all ~42 types of mammalian exocrine glands (*29*), of which the liver is the largest. For example, lactating mammary glands produce milk consistently in the acini, but secretion of milk is induced through the action of hormones such as prolactin on the mammary ducts. From this perspective, the canalicular network may be envisaged as a highly reticulated form of the conventional spheroidal acinus (Fig. 6F). The reticulated geometry is probably imposed due to the necessity of hepatocytes to maximize their contact area with the also reticulated sinusoidal network, which dictates their positioning. This modified acinus is connected to flow-augmented bile ducts in the liver, following the general principle of exocrine glands.

In summary, this work demonstrates the flux mechanisms that operate in the various liver microdomains and provides a generalized methodology to perform quantitative intravital evaluation of flux-associated organ function. The findings here demonstrate the principle of parsimony in action − the energy invested in active transport across membranes is entropically dissipated for canalicular diffusion, to be augmented by energy-driven flow only when this dissipation rate becomes physiologically sub-optimal.

Author contributions

NV and GG performed photoactivation experiments, IVARICS imaging and analysis, and global clearance experiments. NV, GG and AG established methods for intravital imaging. GG performed extrahepatic bile collection and animal handling. ADV generated immunostained 3D confocal z-stacks of mouse livers and digital reconstructions. FJ, IVC, NB, DD developed the in-silico simulations. GW and HH provided harvested liver tissue samples from multiple species. BBT and JGH performed immunohistochemistry of these liver samples. KW, AF, SH performed image analysis and lobular quantification for cross-species comparisons. MR, CH synthesized custom fluorescent bile salt analogs. SJ, FG

provided transgenic reporter mice. FG, HH and PJ provided copious input throughout the research. NV and JGH wrote the manuscript.

Acknowledgment

References

1. N. Vartak, A. Damle-Vartak, B. Richter, O. Dirsch, U. Dahmen, S. Hammad, J. G. Hengstler, Cholestasis-induced adaptive remodeling of interlobular bile ducts. *Hepatology*. **63**, 951–964 (2016).
2. J. L. Boyer, Bile formation and secretion. *Compr. Physiol.* **3**, 1035–1078 (2013).
3. K. Meyer, O. Ostrenko, G. Bourantas, H. Morales-Navarrete, N. Porat-Shliom, F. Segovia-Miranda, H. Nonaka, A. Ghaemi, J.-M. Verbavatz, L. Brusch, I. Sbalzarini, Y. Kalaidzidis, R. Weigert, M. Zerial, A Predictive 3D Multi-Scale Model of Biliary Fluid Dynamics in the Liver Lobule. *Cell Syst.* **4**, 277-290.e9 (2017).
4. S. Afroze, F. Meng, K. Jensen, K. McDaniel, K. Rahal, P. Onori, E. Gaudio, G. Alpini, S. S. Glaser, The physiological roles of secretin and its receptor. *Ann. Transl. Med.* **1**, 29 (2013).
5. T. Saeki, N. Takahashi, R. Kanamoto, K. Iwami, Characterization of Cloned Mouse Na+ /taurocholate Cotransporting Polypeptide by Transient Expression in COS-7 Cells. *Biosci. Biotechnol. Biochem.* **66**, 1116–1118 (2002).
6. M. Kang, C. A. Day, A. K. Kenworthy, E. DiBenedetto, Simplified equation to extract diffusion coefficients from confocal FRAP data. *Traffic*. **13**, 1589–1600 (2012).
7. G. Alpini, Y. Ueno, S. S. Glaser, M. Marzioni, J. L. Phinizy, H. Francis, G. Lesage, Bile acid feeding increased proliferative activity and apical bile acid transporter expression in both small and large rat cholangiocytes. *Hepatology*. **34**, 868–876 (2001).
8. X. Xia, H. Francis, S. Glaser, G. Alpini, G. LeSage, Bile acid interactions with cholangiocytes. *World J. Gastroenterol.* **12**, 3553–3563 (2006).
9. M. J. Rossow, J. M. Sasaki, M. A. Digman, E. Gratton, Raster image correlation spectroscopy in live cells. *Nat. Protoc.* **5**, 1761–1774 (2010).
10. M. A. Digman, E. Gratton, Scanning image correlation spectroscopy. *Bioessays News Rev. Mol. Cell. Dev. Biol.* **34**, 377–385 (2012).
11. J. Hendrix, T. Dekens, W. Schrimpf, D. C. Lamb, Arbitrary-Region Raster Image Correlation Spectroscopy. *Biophys. J.* **111**, 1785–1796 (2016).
12. A. Damle-Vartak, B. Begher-Tibbe, G. Gunther, F. Geisler, N. Vartak, J. G. Hengstler,

Pipe-3D: A Pipeline Based on Immunofluorescence, 3D Confocal Imaging, Reconstructions, and Morphometry for Biliary Network Analysis in Cholestasis. *Methods Mol. Biol. Clifton NJ.* **1981**, 25–53 (2019).

13. P. Carpenter, S. Lindenbaum, Osmotic and activity coefficients of aqueous bile salt solutions at 25, 37, and 45°C. *J. Solut. Chem.* **8**, 347–357 (1979).

14. D. R. de Waart, S. Häusler, M. L. H. Vlaming, C. Kunne, E. Hänggi, H.-J. Gruss, R. P. J. O. Elferink, B. Stieger, Hepatic Transport Mechanisms of Cholyl-l-Lysyl-Fluorescein. *J. Pharmacol. Exp. Ther.* **334**, 78–86 (2010).

15. J. C. Wilton, Fluorescent choleretic and cholestatic bile salts take different paths across the hepatocyte: transcytosis of glycolithocholate leads to an extensive redistribution of annexin II. *J. Cell Biol.* **127**, 401–410 (1994).

16. D. Brogioli, A. Vailati, Diffusive mass transfer by nonequilibrium fluctuations: Fick's law revisited. *Phys. Rev. E.* **63**, 012105 (2000).

17. R. Gallet, C. Violle, N. Fromin, R. Jabbour-Zahab, B. J. Enquist, T. Lenormand, The evolution of bacterial cell size: the internal diffusion-constraint hypothesis. *ISME J.* **11**, 1559–1568 (2017).

18. A. Kaiser, C. J. Klok, J. J. Socha, W.-K. Lee, M. C. Quinlan, J. F. Harrison, Increase in tracheal investment with beetle size supports hypothesis of oxygen limitation on insect gigantism. *Proc. Natl. Acad. Sci.* **104**, 13198–13203 (2007).

19. S.-Y. Cai, X. Ouyang, Y. Chen, C. J. Soroka, J. Wang, A. Mennone, Y. Wang, W. Z. Mehal, D. Jain, J. L. Boyer, Bile acids initiate cholestatic liver injury by triggering a hepatocyte-specific inflammatory response. *JCI Insight.* **2**, e90780 (2017).

20. S. Hoehme, M. Brulport, A. Bauer, E. Bedawy, W. Schormann, M. Hermes, V. Puppe, R. Gebhardt, S. Zellmer, M. Schwarz, E. Bockamp, T. Timmel, J. G. Hengstler, D. Drasdo, Prediction and validation of cell alignment along microvessels as order principle to restore tissue architecture in liver regeneration. *Proc. Natl. Acad. Sci. U. S. A.* **107**, 10371–10376 (2010).

21. R. Lenzen, G. Alpini, N. Tavoloni, Secretin stimulates bile ductular secretory activity through the cAMP system. *Am. J. Physiol.* **263**, G527-32 (1992).

22. G. Alpini, S. S. Glaser, Y. Ueno, R. Rodgers, J. L. Phinizy, H. Francis, L. Baiocchi, L. A. Holcomb, A. Caligiuri, G. D. LeSage, Bile acid feeding induces cholangiocyte proliferation and secretion: Evidence for bile acid–regulated ductal secretion. *Gastroenterology.* **116**, 179–186 (1999).

23. B. Claret, M. Claret, J. L. Mazet, Ionic transport and membrane potential of rat liver cells in normal and low-chloride solutions. *J. Physiol.* **230**, 87–101 (1973).

24. J. M. Banales, J. Prieto, J. F. Medina, Cholangiocyte anion exchange and biliary bicarbonate excretion. *World J. Gastroenterol. WJG.* **12**, 3496–3511 (2006).

25. K. Gupta, Q. Li, J. Fan, E. Li Shan Fong, Z. Song, S. Mo, H. Tang, I. C. Ng, C. W. Ng, P. Pawijit, S. Zhuo, C.-Y. Dong, B. C. Low, A. Wee, Y. Y. Dan, P. Kanchanawong, P. So, V. Viasnoff, H. Yu, Actomyosin Contractility Drives Bile Regurgitation as an Early Homeostatic Response to Increased Biliary Pressure in Obstructive Cholestasis. *BioRxiv* (2016), doi:10.1101/077792.

26. F. Lammert, D. Q.-H. Wang, S. Hillebrandt, A. Geier, P. Fickert, M. Trauner, S. Matern, B. Paigen, M. C. Carey, Spontaneous cholecysto- and hepatolithiasis in Mdr2-/- mice: a model for low phospholipid-associated cholelithiasis. *Hepatol. Baltim. Md.* **39**, 117–128 (2004).

27. P. Fickert, M. Wagner, Biliary bile acids in hepatobiliary injury - What is the link? *J. Hepatol.* **67**, 619–631 (2017).

28. P. Fickert, U. Stöger, A. Fuchsbichler, T. Moustafa, H.-U. Marschall, A. H. Weiglein, O. Tsybrovskyy, H. Jaeschke, K. Zatloukal, H. Denk, M. Trauner, A New Xenobiotic-Induced Mouse Model of Sclerosing Cholangitis and Biliary Fibrosis. *Am. J. Pathol.* **171**, 525–536 (2007).

29. J. Wang, G. W. Laurie, Organogenesis of the exocrine gland. *Dev. Biol.* **273**, 1–22 (2004).

30. R. Reif, A. Ghallab, L. Beattie, G. Günther, L. Kuepfer, P. M. Kaye, J. G. Hengstler, In vivo imaging of systemic transport and elimination of xenobiotics and endogenous molecules in mice. *Arch. Toxicol.* **91**, 1335–1352 (2017).

31. N. B. Javitt, S. Emerman, Effect of sodium taurolithocholate on bile flow and bile acid excretion. *J. Clin. Invest.* **47**, 1002–1014 (1968).

32. J. Kountouras, S. McKavanagh, M. Burmicky, B. H. Billing, The effect of secretin on bile flow and bile acid and bilirubin excretion following relief of prolonged bile duct obstruction in the rat. *J. Hepatol.* **4**, 198–205 (1987).

33. V. Andresen, K. Pollok, J.-L. Rinnenthal, L. Oehme, R. Günther, H. Spiecker, H. Radbruch, J. Gerhard, A. Sporbert, Z. Cseresnyes, A. E. Hauser, R. Niesner, High-Resolution Intravital Microscopy. *PLoS ONE.* **7** (2012), doi:10.1371/journal.pone.0050915.

34. D. L. Kolin, D. Ronis, P. W. Wiseman, k-Space Image Correlation Spectroscopy: A Method for Accurate Transport Measurements Independent of Fluorophore Photophysics. *Biophys. J.* **91**, 3061–3075 (2006).

35. M. J. Rossow, W. W. Mantulin, E. Gratton, Scanning laser image correlation for measurement of flow. *J. Biomed. Opt.* **15**, 026003 (2010).

36. B. Hebert, S. Costantino, P. W. Wiseman, Spatiotemporal image correlation spectroscopy (STICS) theory, verification, and application to protein velocity mapping in living CHO cells. *Biophys. J.* **88**, 3601–3614 (2005).

37. H. G. Weller, G. Tabor, H. Jasak, C. Fureby, A tensorial approach to computational continuum mechanics using object-oriented techniques. *Comput. Phys.* **12**, 620–631 (1998).

38. P. J. Roache, K. N. Ghia, F. M. White, Editorial Policy Statement on the Control of Numerical Accuracy. *J. Fluids Eng.* **108**, 2 (1986).

39. A. Friebel, J. Neitsch, T. Johann, S. Hammad, J. G. Hengstler, D. Drasdo, S. Hoehme, TiQuant: software for tissue analysis, quantification and surface reconstruction. *Bioinforma. Oxf. Engl.* **31**, 3234–3236 (2015).

40. E. P. Martins, T. F. Hansen, Phylogenies and the Comparative Method: A General Approach to Incorporating Phylogenetic Information into the Analysis of Interspecific Data. *Am. Nat.* **149**, 646–667 (1997).

41. F. Madeira, Y. M. Park, J. Lee, N. Buso, T. Gur, N. Madhusoodanan, P. Basutkar, A. R. N. Tivey, S. C. Potter, R. D. Finn, R. Lopez, The EMBL-EBI search and sequence analysis tools APIs in 2019. *Nucleic Acids Res.* **47**, W636–W641 (2019).

42. F. Rodríguez, J. L. Oliver, A. Marín, J. R. Medina, The general stochastic model of nucleotide substitution. *J. Theor. Biol.* **142**, 485–501 (1990).

43. S. Kumar, G. Stecher, M. Li, C. Knyaz, K. Tamura, MEGA X: Molecular Evolutionary Genetics Analysis across Computing Platforms. *Mol. Biol. Evol.* **35**, 1547–1549 (2018).

Figure Legends

Fig. 1. *Definition of diffusion-dominated and advection-augmented compartments of the biliary system and identification of the upper-bound of flux kinetics.* **A**. The diagram depicts the microdomains analyzed in the present study connected to macroscopic structures of the downstream biliary tract. 3D-confocal Z-stacks of HNF1beta/CreER-tdTomato labeled bile ducts (red) and CLF-enriched canalicular network and duct lumen (green) 10 min after tail-vein injection of CLF in live mice. **B.** Representative sequence of repeating CMNB-fluorescein (CMNB-Fluo) photoactivation, with pulses spaced 1.6 s or 223 s apart, showing accumulating fluorescence due to insufficient depletion of a 10 µm×10 µm activation region by canalicular bile flux. The graph shows quantification of intensities, indicating that CMNB-Fluorescein requires >40 s to be cleared from a 10 µm×10 µm region by canalicular flux. **C.** Photoactivation of CMNB-Fluo in the canalicular network and duct showing the activated region (white circle) with its centroid (red, AC), and the distance travelled by the fluorescence fronts (F1, F2) from the centroid due to bile flux. Ducts show vectorial flux (F1>F2) in contrast to symmetric dispersion in the canalicular network (F1~F2). The upper panel shows raw images (green: CMNB-Fluo, red: tdTomato marking ducts) while the lower panel represents the same with a polychromatic color table and annotations. Scale bars: 20 µm. The graphs depict the temporal evolution of spatial intensity profiles after photoactivation, with the intensity centre-of-mass drifting in IBDs but a remaining static in the canalicular network. **D.** Representative images of photoactivation in the PV zone adjacent to a CoH junction (left) and in the CoH junction (right) showing ductular transit and retrograde flux into the canalicular network, respectively. Duct and CoH are annotated as dotted lines. Photoactivated region: White dotted circle. Scale bar: 20 µm.

Fig. 2. **Quantification of canalicular flux in basal and stimulated conditions A.** Stimulation of extrahepatic bile flow after administration of a secretin bolus or TCA infusion. Stimulation was provided 30 min after extrahepatic bile collection started (arrow). Data indicated mean ± S.D of 3 mice per condition**. B.** Representative time-lapse images following photo-activation in a defined region (white circle) of CMNB-Fluo (green) in canalicular networks adjacent to the central vein (CV), portal vein (PV) or in the mid-zone (MZ), as well as in interlobular bile ducts marked by tdTomato (red). Scale bars: 50 µm. **C.** Quantification of diffusion coefficients from the half-life of intensity decay and advection velocity from shift of intensity centre-of-mass for various lobular zones (CV: pericentral; MZ: midzonal; PV: periportal) under basal conditions or stimulation with secretin and TCA. Values indicate measurements in n>8 mice for each condition. Dots in the box plots represent the data of individual mice. **p<0.01 compared to controls.

Fig. 3. *Establishment of IVARICS* **A.** Representative images acquired for ICS analysis in canaliculi, hepatocyte cytoplasm and sinusoids. The graph shows quantification of diffusion coefficient and velocity in each compartment. **B.** Workflow of IVARICS analysis. Representative fluctuation images of fluorescein loaded canaliculi and ducts are acquired. A binary mask representing the structures of interest is created. Autocorrelation (ACF) maps are generated for both the intensity images and masks. A ratio of the intensity ACF and mask ACF yields a fluctuation ACF devoid of movement and shape effects. **C.** Average normalized spatial (y)-autocorrelation for various liver domains with fits for 1-population 3D-diffusion. **D.** Average normalized temporal autocorrelation for various liver domains with fits for 1-population 3D-diffusion and advection.. **E.** Diffusion coefficients and velocities derived from spatial (RICS) and temporal (TICS) analysis for various canalicular zones (green) and

17

interlobular bile ducts (red) under basal conditions or stimulation with secretin and TCA. Values indicate measurements of n>4 mice for each condition. The dots in the box plots represent the data of individual mice. **p<0.01 compared to controls.

Fig. 4. *Simulation of bile acid flux mechanisms* **A.** Representative 3D immunostained confocal stack (left) identifying the canalicular network and interlobular bile duct and its digitization to a polygonal mesh (right). **B.** Simulation of repeated photoactivation with various time intervals in a 10 µm radius spherical region encompassing a canaliculus. Graphs show quantification of mean intensity in the activated spherical region with various activation intervals (compare: Fig. 1B). **C.** Simulation of single photoactivation in the canalicular network of varying radii (top, middle) and interlobular ducts (bottom), showing directional shift in the center of mass of the spatial intensity. Graphs show temporal profiles in the canalicular network (compare: Fig. S1B), spatial profiles in the IBD and canalicular network (compare: Fig. 1C). **D.** Simulation of photoactivation in the Canal of Hering, showing retrograde diffusion to the canalicular network (compare: Fig. 1D). All simulations were performed with experimentally derived flux parameters (D = 3 μm^2/s, V = 0 µm/s in canaliculi, 1 µm/s in ducts). Photoactivated region: White dotted circle. Scale bar: 10 µm.

Fig. 5. *TCA, secretin and cholate do not influence canalicular clearance* **A.** Representative time-lapse images of the canalicular clearance of CLF with and without TCA infusion. **B.** Representative time-lapse images of the canalicular clearance of CLF with and without secretin administration. **C.** Representative time-lapse images of the canalicular clearance of fluorescein with and without cholate injection. **D.** Quantitative comparison of clearance kinetics under conditions described in A, B, C, for n > 6 mice each, with no significant

difference due to secretin, TCA or cholate treatment for the respective fluorophore. Scale bar: 50 μM.

Fig. 6. Size *restriction of liver lobules across species.* A. Workflow of immunohistochemistry to identify central veins, lobule boundary identification and quantification of liver samples from multiple species. **B**. Phylogenetic generalized least squares analysis for correlation of body weight across species to liver weight, lobular area, nuclear diameter and cell density. **C**. Scatter plot showing that liver weight increases proportionally with body weight over 5 orders of magnitude, while lobular area increase is restricted to ~1 order of magnitude over the same range. **D**. Scatter plot showing no increase in nuclear diameter or cell density in species with increasing body weight. **E.** Schematic representation of the diffusion-dominated domain, the canalicular network and the advection-augmented domain, the interlobular bile duct in the liver. Bile acids (BA) are secreted in the diffusion-dominated zone, while water is secreted in the advection-augmented zone. **F.** Comparison of liver tissue topography to that of a generic exocrine gland in terms of solute secretion zone and water secretion zone, implying that the liver canalicular network is analogous to an exocrine acinus, only modified geometrically from a sphere to a reticulated network.

19

Supplementary Information

Materials and Methods

Animal handling and preparation for microscopy

Animal preparation for intravital imaging was performed according to a published method (*30*). Briefly, mice were anaesthetized with a combination of ketamine (64 mg/kg), xylazine (7.2 mg/kg) and acepromazine (1.7 mg/kg) given intraperitoneally. The abdomen of the animal was shaved, and a ~1.5 cm midline incision made to expose the xiphoid process which was retracted to allow dissection of the falciform ligament. The left lobe of the liver was gently exteriorized, and the animal inverted onto a 49 mm x 74 mm glass coverslip of 0.17-0.16 mm thickness (Ocon 159, Logitech, Glasgow, UK) mounted within a custom-made imaging platform. The liver was covered with sterile saline-soaked gauze to prevent dehydration. Additionally, a subcutaneous injection of 0.5 ml saline was given. During imaging mice were kept under ongoing anesthesia of 1-2% isoflurane in a climate-controlled chamber.

Male C57BL/6N mice, 8-10 weeks old were obtained from Charles River (Sulzfeld, Germany), HNF1beta/CreER-reporter mice were obtained from Dr. Fabian Geisler. All experiments were approved by the local animal protection agency.

Intravenous administration

Bolus injection

1. CLF (Corning, Product no. 451041), fluorescein (Thermo-Fischer Scientific, Cat no. F1300) and CMNB-Fluorescein (Thermo-Fischer Scientific, Cat. no. C20050) were dissolved in phosphate-buffered saline (PBS) to a concentration of 1 mg/ml and administered intravenously through a tail-vein catheter at a dose of 1 mg$\times$kg^{-1}.

2. Lyophilized human Secretin (TOCRIS, Cat. No. 1918) was dissolved in PBS to a concentration of 75 U/ml and administered intravenously through a tail-vein catheter into mice at a dose of 3.0 U$\times$kg^{-1}.

Infusion

For experiments involving infusion, intravenous tail-vein catheters in mice were infused via a syringe pump (Perkin-Elmer).

1. CLF and fluorescein were dissolved to a concentration of 1 mg/ml in PBS and infused at a rate of 50 $\mu L \times kg^{-1} \times min^{-1}$.

2. TCA (Sigma-Aldrich, Cat. no. 86339) was infused at a rate of 660 $nmol \times kg^{-1} \times min^{-1}$ (*31*). The total infused volume was not allowed to exceed 200 μL.

Extrahepatic bile collection

Collection of extrahepatic bile was achieved by ligation of the common bile duct, followed by catheterization of the extrahepatic bile duct just before it enters the gall bladder fundus (*32*). Bile was collected from anaesthetized mice, with or without secretin/TCA administration, in pre-weighed Eppendorf tubes and the quantity collected was measured every 10 minutes.

General imaging setup

Imaging was performed on a Zeiss LSM 880 confocal microscope equipped with a 40×N.A 1.4 PLAN-APOCHROMAT oil-immersion objective, 2 GaAsP and 1 PMT detector, an automated stage and climate-control chamber. Excitation was achieved with the Argon 488 laser line for CLF, fluorescein and CMNB-fluorescein, the HeNe 561 line for tdTomato. Emission bands for CLF, fluorescein and CMNB-fluorescein were set at 498-551 nm, while 571-630 nm were used for tdTomato. Imaging resolution was set at 512 × 512 pixels, with 8-bit acquisition depth and a frame rate of 1s.

Photo-activation

Imaging

Photoactivation of CMNB-Fluorescein was performed with a 405 nm diode laser in a manually defined circular ROI of 5-40 μm radius. Typical in vivo photoactivation

sequences consisted of images acquired without activation for 5 frames at 1s/frame, followed by 2s of photoactivation in the ROI and subsequent imaging for 5 min at 1s/frame. For in vitro photoactivation, 10 μm CMNB-Fluorescein was dissolved in distilled water or mouse bile (collected as described above) and frame times were reduced to 100 ms/frame to compensate for the faster diffusion of small molecules in water.

Analysis

1. *Diffusion*

The centroid of the photoactivated area was identified using 1D-line profiles of the first photoactivation image in x and y. Gaussian fitting of these line profiles was used to identify the full width half-maximum (FWHM) of the profiles in X and Y.
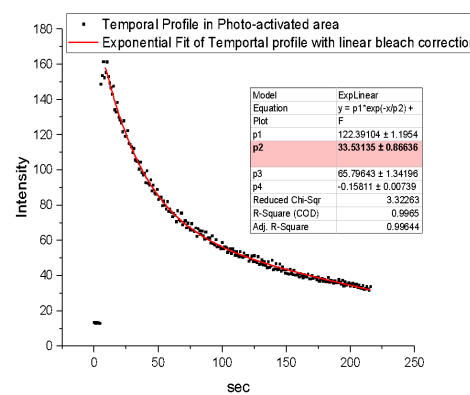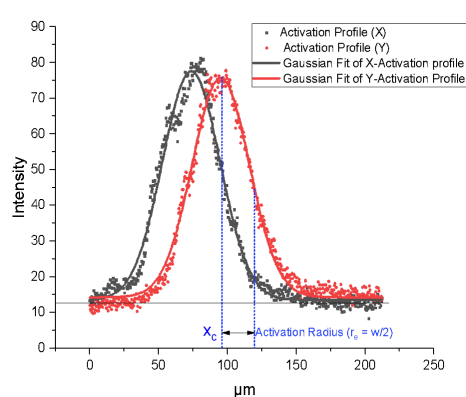
The effective radius r_e was taken as FWHM/2. Nominal radius r_n corresponds to the user-defined photoactivation area and was derived directly from instrument metadata.

For determination of half-life, the temporal decay of mean intensity in the activated area was measured and fitted to a mono-exponential decay and linear function. The linear function accounted for bleaching that may occur over the monitoring interval.

$$I_t = I_{t=0} . e^{\frac{-t}{\tau}} + bt + C$$

22

$$\tau_{1/2} = ln(2) \times \tau$$

where I_t is the intensity at time t, and b is the bleaching constant, C is the offset in intensity, τ is the exponential time constant and $\tau_{1/2}$ is the half-life of decay. The diffusion coefficient, D, was then determined using the Soumpasis method (6) as:

$$D = \frac{r_n^2 + r_e^2}{8\tau_{1/2}}$$

2. *Advection*

In order to determine advection velocity, the location of the centroid of intensity in the spatial activation profiles (see above), were obtained over all frames in a time-lapse sequence, following photoactivation. The mean-square displacement of the centroid per unit time gave the velocity v per frame.

$$v = \frac{\sqrt{(x_{c,t} - x_{c,0})^2 + (y_{c,t} - y_{c,0})^2}}{\Delta t}$$

Where x_c and y_c are the location of the centroids at time t and t=0 and Δt is the time between frames. The mean velocity over all the frames in the time-lapse sequence was derived and reported.

Analysis for performed using FIJI/ImageJ (http://www.fiji.sc) through manual tracking of the fluorescence centroid over time for advection velocity, and determination of intensity decay over time to determine a half-life and area of activation for diffusion coefficients.

IVARICS

Theory

Spatial and Temporal Image Correlation Spectroscopy (RICS/TICS) is part of a family of methods where the autocorrelation of fluorescence signals is analysed to extract information regarding molecular events. Fundamentally, the magnitude of autocorrelation decays in time as molecular events progressively change the distribution of fluorophores, i.e, decorrelates them.

ICS exploits the raster imaging design of a confocal scanning microscope, wherein pixels are acquired sequentially to form a line, lines are acquired sequentially to form an image and images are acquired sequentially to produce a stack. Thus, the temporal autocorrelations in time produced by underlying molecular events are encoded in the spatial dimensions of the image (or stack). Autocorrelation (G (x,y,t)) curves obtained over space can then be used to derive information about the molecular processes involved.

The generalized discrete normalized spatiotemporal autocorrelation function for a fluctuating signal I with dimensions X, Y, T is defined explicitly as:

$$G(\varepsilon, \psi, \tau) = \frac{\langle \delta I(x,y,t) \times \delta I(x+\varepsilon, y+\psi, t+\tau) \rangle}{\langle I(x,y,t) \rangle^2} =$$

$$G(\varepsilon, \psi, \tau) = \frac{\sum\limits_{x=1}^{X} \sum\limits_{y=1}^{Y} \sum\limits_{t=1}^{T} \delta I(x,y,t) \times \delta I(x+\varepsilon, y+\psi, t+\tau)}{(X-|\varepsilon|)(y-|\psi|)(t-|\tau|)} \times \left(\frac{XYT}{\sum\limits_{x=1}^{X} \sum\limits_{y=1}^{Y} \sum\limits_{t=1}^{T} I(x,y,t)} \right)^2$$

where the fluctuation $\delta I(x,y,t)$ is the deviation from the mean $I(x,y,t)$ of the signal I:

$\delta I(x,y,t) = I(x,y,t) - E(I(x,y,t))$

ε, ψ, τ are the correlation lags and E(I(x,y,t) represents the mean intensity of the pixels in dimensions X, Y and T, respectively.

Considerations for in vivo ICS imaging

The precise magnitude and shape of the autocorrelation function during in vivo imaging is affected by several experimental and mechanistic parameters. These parameters, and procedural aspects for each of the methods is described below.

- Concentration of fluorophores: The magnitude of the autocorrelation function G varies inversely with the number of molecules (N). The measured autocorrelation is scaled by (1/N). The in vivo concentration of fluorophores in liver canalicular compartments is largely determined by the amount injected into the animal and the degree by which hepatocytes take up the fluorophore from the blood and export it into canaliculi.

- Fluorophore intermittency: Most molecular fluorescent emitters switch between bright and dark states intermittently at timescales of a few seconds. Since the pixel acquisition times utilized in RICS typically range from 2-32 μs, RICS sequences are not significantly affected by fluorophore blinking.

- Binding events: As most fluorophores are hydrophobic to some degree, molecular binding events with hydrophobic structures such as membranes occur in biological samples. These events typically reduce the mobility of the fluorophore, and in the present work are assumed to affect molecular flux, which may influence the apparent diffusion coefficient.

- Instrumental correlations from detector noise: Dark current in detectors used on confocal microscopes is usually correlated and may contribute to the autocorrelation. The absence of correlated dark current-related noise in the GaAsP detector used in our setup was confirmed by acquiring image sequences without laser illumination and confirming that the autocorrelation function has a value of 0 across all pixel lags. Shot noise from the detector is easily eliminated by excluding the (0,0) point from the RICS fitting.

- Instrumental correlations due to scanner movement: The regular movement of the scanner creates autocorrelation that is convolved with the autocorrelation due to molecular fluctuations. Ths autocorrelation due to the scanner movement is given as:

$$S = e^{-\left\{\left[\left(\frac{|\varepsilon|\delta x}{\omega_0}\right)^2 + \left(\frac{|\psi|\delta y}{\omega_0}\right)^2\right]\left(1 + \frac{4D(\tau_x\varepsilon + \tau_y\psi)}{\omega_0^2}\right)^{-1}\right\}}$$

where ω_0 is the beam-waist in x and y,

ε and ψ are the spatial lag in pixel in x and y respectively,

δx and δy are the pixel dimensions in x and y respectively,

D is the diffusion coefficient,

τ_x and τ_y are the pixel-dwell times and line times in x and y respectively.

- Instrumental PSF size and shape: Confocal point-spread functions (PSFs) are theoretically expected to be an elliptical 3D Gaussian, which is symmetric in the x and y directions (beam-waist) and elongated in the z-direction (axial distance). The dimensions by which the PSF affect the autocorrelation function are accounted for by the ω_0 and ω_z parameters representing the beam-waist and axial-distance, respectively. For measuring autocorrelation, it is necessary to set the pixel dimensions δx and $\delta y <$ ω_0.

In practice, the PSF may also be asymmetric due to inconsistencies in component manufacturing or beam alignment of the microscope. These asymmetries are represented as a shape-factor γ. For a theoretical confocal PSF, $\gamma = 2^{(-3/2)} = 0.3535$, and ω_0 and ω_z are in the range of 0.4μm and 0.8 μm at the focal point. However, these parameters are substantially affected during in vivo imaging due to tissue scattering, with beam-widths expanding upto 4-fold and 5-fold in the (x,y) and (z) directions respectively (33). Since it is not possible to precisely determine the changes in these parameters in a live animal during intravital imaging, ω_0 and ω_z are left as free parameters with constraints rather than as fixed parameters during fitting (see below).

- Presence of immobile or slowly moving populations: Slow moving structures or immobile populations which display little to no fluorescence fluctuations can significantly affect the autocorrelation function by artificially stretching the

autocorrelation curve. The influence of these structures is corrected by subtracting the moving average of the stack from each frame, and rescaling the autocorrelation function. This operation represents a high-pass filter that removes slow or zero fluctuations from the image sequences.

The moving average for a raw intensity image at time t is defined as:

$$I_{corr}(x,y,t) = I(x,y,t) - (2\Delta F+1)^{-1} \sum_{-\Delta F}^{\Delta F} I(x,y,t)_F + \langle I \rangle_{XYT}$$

where I(x, y, t) is the frame F at time t, ΔF is the moving average window size, and $\langle I \rangle_{XYT}$ is the average intensity of the entire stack.

The autocorrelation function G obtained from $I_{corr}(x,y,t)$ is re-scaled to compensate for the net reduced intensity due to the subtraction of the mean as follows:

$$G_{corr} = \frac{2\Delta F+1}{2\Delta F} G$$

For all experiments in the present work, we used the moving average window size of $\Delta F = 1$.

- Animal movements: In vivo imaging sequences are affected by movements in the organ of interest in the animal due to breathing, heart rate and intestinal peristalsis. These movements typically occur in the range of 14 ms -1s in a mouse.

To avoid these artifacts in the spatial autocorrelation, we restricted the maximum pixel acquisition time to 8 μs, and the maximum image acquisition time to 250 μs. Since these movements occur on a slower timescale compared to molecular fluctuations, the high-pass filter applied to remove slowly moving structures effectively filters of the effect of animal movements.

The temporal autocorrelation of the images is more significantly affected by animal movements despite correction by moving average filtering. Due to their periodic nature animal movements manifest as recurring spikes in the temporal autocorrelation of a stack, despite a general decay in the correlation amplitude. A band-pass FFT filter of frequency equivalent to 1/4Δt was applied to compensate for animal movements, where Δt is the time lag between frames (Fig. S2). Utilization of such a filter,

27

however, can have the undesirable outcome of removing the autocorrelation decays of the flux processes we are interested in. As a result, the filter must be applied judiciously, manually and only ICS sequences where mouse movement occurs at frequencies different from the fluctuation frequency were further analyzed.

- Irregular regions of interest: Generally, ICS is performed on square regions where the number of times a particular spatial lag is sampled is a linear function. Since the liver canalicular structures and bile ducts measured are not conducive to assigning square regions due to their irregular shape, we adapted the Arbitrary region RICS algorithm (ARICS) (*11*), wherein the autocorrelation function G in a particular irregular structure is normalized to the number of times each spatial lag is sampled by calculating the autocorrelation of a binary mask of the irregular structure.

In our case, time-lapse sequences were then thresholded for fluorescent structures representing the canalicular network or interlobular ducts to obtain the respective binary masks. Spatial autocorrelation maps were calculated from the binary masks containing exclusively the 'shape-autocorrelation' without information on the flux. According to the ARICS algorithm, these sets of autocorrelation maps were then used to derive the autocorrelation representing only the fluorescence fluctuation due to the flux mechanism, as follows:

- High-pass filter for removal of slow/immobile structures with $\Delta F = 1$ was applied to obtain the corrected RICS sequence.

- For each frame image I, a binary mask M was generated using Otsu thresholding, where areas representing the biological structure of interest were valued as 1, while the background was valued as 0.

- The masked image $(I \times M)$ was computed through pixel-wise multiplication of I and M.

- The fluctuation image F can now be defined as the element difference of all non-zero pixels in $I \times M$ and the mean of all non-zero pixel in $I \times M$:

28

$$F = \{I \times M\} - \overline{I \times M}$$

- To avoid boundary and aliasing effects, M and F were 0-padded with $(2 \times$ dimension $+ 1)$ zeros in the x,y, and z dimensions and the autocorrelation $A(M)$ and $A(F)$ was calculated using the Wiener–Khinchin theorem. Briefly, the autocorrelation of a function is the **real part** of the **product** of the **Fourier transform of the function** with the **complex conjugate of the Fourier transform of that function**.

$$A(X) = REAL\ [\ FFT(X)\ *\ CONJ(FFT(X)\ ]$$

- The unnormalized autocorrelation due to fluctuation G is now defined as:

$$G = \frac{A(F)}{A(M)}$$

- To obtain the spatial autocorrelation function: G_{RICS} , the spatial autocorrelation at each time point is normalized with the average squared intensity of the pixels in $(I \times M)$ at that time point. The spatial autocorrelations for all frames are averaged to obtain the normalized autocorrelation function G_{norm}.
- G_{norm} is rescaled to correct for moving average subtraction (as stated above) to obtain the final autocorrelation function G_{RICS}.
- To obtain the temporal autocorrelation function G_{TICS}, the value of G at spatial lag (0,0) was calculated as above and normalized by the average squared intensity of every pixel in $(I \times M)$ over the entire stack.

The spatial autocorrelation in the y-direction was utilized due to few pixels in the x-direction for canaliculi, and was fitting to a 1-population 3D-diffusion function. The temporal autocorrelation was fitted to a 1-population 2component diffusion and velocity function.

29

<u>Limitations of ICS for in vivo imaging</u>: While ICS represents a powerful method for accessing molecular flux mechanisms in live animals, we encountered several challenges in its application. These are summarized below:

1. A priori knowledge: ICS sequences require some knowledge of the range in which flux is expected, as image acquisition parameters are set accordingly. For a given set of image acquisition parameters, it is possible that faster and slower autocorrelations arising from different populations are not represented well in the experimental autocorrelation decay. In the case of in vivo imaging, where biological fluids typically contain multiple diffusing populations, ICS yields only an apparent diffusion coefficient. Further, as in our case, a balance has to be struck between imaging speeds that allow measurement of the autocorrelation decay of molecular flux, while avoiding the effect of animal movements that occur over longer time periods. This is not always possible.

2. Dependence on non-linear fitting: ICS data provides diffusion coefficients and advection velocities from non-linear fitting of the autocorrelation decay. Diffusion results in hyperbolic autocorrelation decays, while advection results in Gaussian autocorrelation decay (*34*). An experimental in vivo autocorrelation curve with diffusion and velocity is therefore a convolution of hyperbolic and Gaussian decays Fitting of these curves is non-trivial and requires the utilization of global fitting procedures for a robust fit.

3. Structure effects: The geometry of the structure in which flux occurs also affects the autocorrelation function. In relevance this work, a single canaliculus is a tubular structure of only upto 0.8 μm in diameter, but extending upto 15 μm in length. Thus, the number of pixels along the diameter is much fewer and usually not sufficient to obtain a good autocorrelation function, restricting us to using the line correlation instead for RICS analysis (*35*). Further, the geometry of the biological structure may also affect

4. Requirement of a representative model: The autocorrelation decays are affected by several parameters such as binding and unbinding, number of populations with flux and the flux speeds, geometry of the

30

Imaging and Preprocessing

In addition to standard imaging parameters described previously, the following specific imaging parameters were: pixel dwell-times ranging from 2-32 µs, and pixel sizes adjusted for 2-4× oversampling in XY. Microscope pinhole size was adjusted to provide a confocal Z-depth that encompasses the canaliculi (~0.5 µm). Rapid scanning was performed for 20 frames.

Typical representation of metadata relevant for IVARICS is provided below:

File format: CZI

Dimensions - X: 128.0 Y: 128.0 T: 20.0

Pixel size: 1.66053164193e-07 m

Pixel dwell-time: 8.24242424242e-06 s

Scan line time: 0.00108503030303 s

Frame time: 0.316509090909 s

PSF - beam waist: 324.676083907 nm

PSF - axial distance: 865.238181818 nm

Raw image stacks were processed for removal of immobile populations and assigning arbitrary regions for analysis as described above.

Analysis of Molecular Flux by Diffusion and Advection

Fluctuations of the fluorophore intensity at each pixel occur due to molecular flux of fluorophores. Autocorrelation in these fluctuations over time and space can be used to compute diffusion coefficients and advection velocities through ICS analysis (*36*).

For a single population of fluorophores with diffusion and advection, the spatial autocorrelation due to diffusion is given as:

31

$$G(\varepsilon, \psi, 0) = (\gamma/N) \times \left(1 + \frac{4D(\tau_x\varepsilon + \tau_y\psi)}{\omega_0^2}\right)^{-1} \times \left(1 + \frac{4D(\tau_x\varepsilon + \tau_y\psi)}{\omega_z^2}\right)^{-1/2}$$

The temporal autocorrelation of the image sequence is given as:

$$G(0, 0, \tau) = G(0, 0, 0) \times \left(1 + \frac{4D\tau}{\omega_0^2}\right)^{-1}\left(1 + \frac{4D\tau}{\omega_z^2}\right)^{-1/2} \times e^{-\left\{\left[\left(\frac{v\tau}{\omega_0}\right)^2\right]\left(1 + \frac{4D\tau}{\omega_0^2}\right)^{-1}\right\}} + G(\infty)$$

where ω_0 is the beam-waist in x and y, and ω_z is the axial distance

ε and ψ are the spatial lag in pixel in x and y respectively,

δx and δy are the pixel dimensions in x and y respectively,

τ_x and τ_y are the pixel-dwell times and line times in x and y respectively,

τ is the lag time between frames,

γ is the PSF shape factor,

N is the number of fluorescent entities per PSF,

D is the effective diffusion coefficient,

and v is the advection velocity.

Flux parameters can be independently derived from the spatial and temporal ICS sequences through fitting of the spatial autocorrelation maps for each frame as:

$G_{RICS} = G(\varepsilon, \psi, 0) \times S$ for diffusion coefficient D

$G_{TICS} = G(0, 0, \tau)$ for diffusion coefficient D and advection velocity v

To prevent bias from the strong correlation at G (0,0) due to shot noise, the ε, $\varphi = 0$ points were excluded from fitting.

Python code for the functions computing the above parameters and extracting relevant metadata from the raw image files is provided as a Python scripts **RICSAnalysis.py and TICSAnalysis.py** (see Appendix).

Generation of an instrument calibration curve

In order to generate instrument calibration curves, we collected bile from mice and dissolved varying concentrations of CLF (0-700 µM) in mouse bile. These solutions were then imaged under our intravital imaging conditions in 8-well glass-bottom dishes (ibidi) at multiple locations per well. Mean intensities of the images acquired per concentration of CLF were then utilized to plot the calibration curve.

In silico modeling

1. Digitization of liver tissue geometry

Mouse liver tissue slices of approximately 70 µm thickness were fixed and immunostained with Alexa 488-labeled anti-DPP4 and Alexa 594-labeled anti-KRT19 antibodies as described previously (*12*). DPP4 is a marker for apical membranes and allows visualization of canaliculi. KRT19 is a cholangiocyte specific marker that allows visualization of interlobular bile ducts. Confocal Z-stacks were obtained using imaging parameters as described earlier and Z-stacks were segmented to obtain specific canalicular and duct signals (ImageJ). The volume of the reconstructed isosurface of the reconstructed canalicular network and ducts was then discretized in a polyhedral mesh with 1.75 million volume elements ("cfMesh", Creative-Fields, UK). The outer surface was divided into three sub-domains: the inlet and outlet of the bile duct and the wall of the bile duct and bile canaliculi.

2. Molecular transport simulation in bile

Theoretical considerations

Molecular transport in bile was modelled by an advection-diffusion equation. For a species of concentration $c(\underline{x}, t)$ (*t*=time, $\underline{x}$=space vector) this equation reads:

$$\frac{\partial c}{\partial t} + \underline{\nabla} \cdot (\underline{v}c) = \underline{\nabla} \bullet (D\,\underline{\nabla}c) \,.$$

D is the diffusion coefficient and assumed to be constant. The local velocity vector field $\underline{v}(\underline{x}, t)$ has been determined from the Navier-Stokes equation of an incompressible Newtonian fluid:

$$\rho \left(\frac{\partial \underline{v}}{\partial t} + (\underline{v} \bullet \underline{\nabla}) \underline{v} \right) = - \nabla p + \mu \underline{\nabla} \bullet \underline{\nabla v}.$$

where $\rho(\underline{x},t)$ is the local fluid density, $p(\underline{x},t)$ is the hydrostatic pressure, and μ is the dynamic viscosity. Incompressibility implies $\underline{\nabla} \bullet \underline{v} = 0$ from the mass conservation, steady state implies $\frac{\partial (\ldots)}{\partial t} = 0$.

Numerical implementation

The time-independent flow was computed by solving the stationary incompressible Navier-Stokes equations using the finite-volume methods implemented in the OpenFOAM toolbox (*37*). A large time-step transient solver was used to solve the pressure–velocity coupling, the PIMPLE (merged PISO-SIMPLE) algorithm. Spatial convergence was checked computing the Grid Convergence Index (GCI) (*38*) and the numerical convergence was ensured. The flow velocity was fed into a transient advection-diffusion equation for the concentration of labeled molecules. In order to minimize numerical diffusion and precisely capture the diffusion process, a *SuperBee* flux-limiter was used.

The diffusion simulations (for *v=0*) in continuum space were verified against particle-based simulations in one-, two-, and three dimensions in a stochastic compartmental approach on a regular lattice (solving a multivariate master equation) with various initial activation zones and analytical results in those settings that were amenable to analytical solution.

Simulation

Bile was considered as a Newtonian fluid of a *10^6 $\mu m^2/s$* viscosity and the molecular diffusion coefficient in bile was set to 3 $\mu m^2/s$, the in vivo diffusion coefficient of bile salts determined experimentally. A fixed bile velocity was imposed normal to the inlet of the bile-duct, set as *1 $\mu m/s$,* the in-plane components being set to zero, and a fixed pressure was constrained at its

exit. A non-slip condition ($v=0$) was chosen for the flow at the walls. For the concentration, a no-gradient boundary condition was set on all the boundaries.

The following situations of particular interest were then simulated:

- Repeated activation (Fig. 4B): At activation times $t=k\ t_a$, (n see Fig. 4B), c was elevated by a constant value c_0 in the activated zone.

- Activation experiments in Fig. 4C, D (BC=bile canaliculi): At $t=t_0=0$, c was set to a constant value c_0 in the activated zone. The activated bile salt concentration value was without loss of generality fixed as initial condition at $c_0=10^6\ M$ in the chosen activation zone of the bile canaliculi and $0\ M$ elsewhere.

  1. $R=5\ \mu m$ radius spheres in the BC: Decay of a sphere of radius $=5\ \mu m$ at approximately $30\ \mu m$ Euclidian distance from the BD, $T_{1/2}=5.5$ s;

  2. $R=10\ \mu m$ radius spheres in the BC: Decay of a sphere of radius $=15\ \mu m$ in a midzonal canalicular region, $T_{1/2}=15.75$ s;

  3. $R=5\ \mu m$ spheres at the interface between canaliculi and duct (CoH) with $1\ \mu m/s$ inflow in the BD: Decay of a sphere of radius $=5\ \mu m$ at the interface between canaliculi and duct (CoH), $T_{1/2}=2.28\ sec$. The speed of advection in the duct is $1\ \mu m/sec$ and virtually 0 in the BC, hence in-between in the CoH.

The half-life times in cases (1.) and (2.) are between the value obtained for pure diffusion for a 1d domain and a 2d domain in a homogeneous isotropic medium: In a 1-dimensional homogeneous, practically infinite domain with initial condition $c(x,t=0)=c_0 >0$ in $-R \leq x \leq R$ (R: radius), $c_0 =0$ otherwise, the half-life time has been numerically determined as: $T_{1/2} \approx \frac{0.956}{D}R^2$, i.e. $T_{1/2} \approx 7.96\ sec$ for R=5μm and $T_{1/2} \approx 31.87\ sec$ for R=10μm.

In a 2-dimensional homogeneous, isotropic, practically infinite domain with initial condition $c(r, t=0)=c_0 >0$ in $-R \leq r \leq R$ (r being the radius around the origin at $(x,y)=(0,0)$ in polar coordinates), $c_0 =0$ otherwise, the half-life time has been numerically determined as $T_{1/2} \approx \frac{0.229}{D}R^2$ (6), i.e. $T_{1/2} \approx 1.91\ sec$ for R=5μm and $T_{1/2} \approx 7.63\ sec$ for R=10μm.

Simulations in which the diffusing species reaches the impermeable domain border before the concentration in the activated domain has dropped to half of its initial value (i.e., $c_0/2$), were not utilized. Moreover, we found that the mean-square displacement on a 2-dimensional

square network is between the mean-square displacement of a 1 dimensional homogeneous domain, and a 2 dimensional homogeneous, isotropic domain, consistent with the findings for cases (1.) and (2.) above.

- Activation in the bile duct (Fig. 4C): The BD in the domain was elongated towards the same length as in the experiment. The initial value $c(\underline{x},t=0)$ was extrapolated from the experimental results: 1) a Gaussian function was fitted on the experimental curve $c(x,t=0)$ (Fig 1C, bottom) and 2) this curve was imposed in the bile along the main axis of an equivalent cylinder (x being the coordinate along this axis; the concentration is constant within each cross-section to this axis). Data was sampled along the centerline of arclength s of the duct for post-processing. For the activation in the bile canaliculi (Fig. 4C) the initial concentration profile was determined as for the BD and the simulation executed as explained for Fig. 4D.

36

Cross-species liver lobule analysis

Formalin fixed paraffin embedded liver tissue from 29 mammalian species was obtained from a collection of the Leibniz Institute for Zoo and Wildlife Research (Berlin, Germany), from local slaughterhouses and from Charles River (Sulzfeld, Germany); (documentation of all samples and staining results: Table S1). Immunostaining of glutamine synthetase (GS) was performed using a published protocol (*12*). Two tissue slices of the different species were incubated with one of the two antibodies each, Life Span BioSciences, inc (LS-B2579), dilution 1:500; and Sigma-Aldrich (G2781), dilution 1:5,000. Staining with these two antibodies allowed visualization of pericentral hepatocytes in 24 species that were further evaluated in the results, while no sufficient staining was obtained in 5 species. The area of the lobules was analyzed after reconstruction using the watershed algorithm as described in Friebel et al, 2015 (*39*). Nuclear size and density were determined after segmentation of the hematoxylin signal similar as described in Hoehme et al, 2010 (*20*). To reduce bias due to the section plane, lobules with longitudinally cut central veins were excluded by the algorithm.

Image Processing Methods

Given a bright-field liver tissue scan stained as described above all central and portal veins are marked manually in a first step. Using these two sets of seed points a region growing algorithm as applied to generate segmentations of the central and portal vein lumen. Subsequently, for every non-lumen pixel its shortest Euclidean distance to the closest central respectively portal vein lumen pixel was calculated. This tuple of distances was used to compute a gradient value for each pixel. A variant of the watershed algorithm (*20, 39*) was then applied to the gradient image to generate an approximation of lobule shapes. Lobules with an area smaller than 0.032 mm^2 were discarded automatically, before lobule approximation quality was manually assessed. For visual inspection lobule boundaries were shown in an overlay image directly in the original scan. Some lobules were manually removed and thus not considered for analysis if at least one of the following conditions was met: tissue within the lobule was damaged due to processing artefacts, lobules contained tangentially cut veins; lobules were artificially clipped, e.g. by a tissue border. Finally, all remaining lobules were quantified with regard to their area (in μm²).

37

Nuclei Density Analysis

Analysis of nuclei density and related measures required segmentation of the nuclei, as well as background (i.e. non-tissue) and GS-positive areas. A basic processing procedure composed of initial thresholding was applied, operating in the RGB and HSV color spaces, followed by hole filling as well as morphological closing and opening operators as optional post-processing steps. Thresholds were manually determined for each of the six channels of the RGB and HSV color spaces, although in most cases only a subset of channels was used. The background and GS-positive area segmentations were combined yielding a mask for the GS-negative tissue areas that were considered for analysis (ROI). During visual examination of nuclei segmentation quality, regions with local deficiencies were manually removed from the ROI. This encompasses regions that suffered from at least one of the following criteria: damaged tissue, atypical tissue states (e.g. massive fat droplet accumulation, areas with infiltration of immune cells, necrotic tissue) and sub-optimal staining quality. All segmented nuclei in the ROI were analyzed for their area and diameter (assuming perfect roundness). Additionally, the overall number of nuclei, their accumulated area, the area of the ROI, the nuclei density (number of nuclei per mm²) and the ratio of total nuclei area to ROI area were determined.

Anatomical Data

Body mass of the different species was obtained from the Quaardwark database of the University of Michigan (https://animaldiversity.ummz.umich.edu/quaardvark/). For species without information available in the Quaardwark database, body mass data were obtained from the references given in Table S1. Liver mass was obtained from the references listed in Table S1.

Phylogenetic statistics and analyses

The possible association of body weight with liver weight, lobule area, diameter of hepatocyte nuclei and nuclei density were assessed with phylogenetic generalized least squares (PGLS), thereby taking the possibility of similarities because of phylogenetic relatedness into account (Ridley 1983, Felsenstein 1985). PGLR was conducted in R version

3.6.1 (R Core Team 2019) using packages *ape* v. 5.3 (Paradis 2006) and *nlme* v. 3.1-140. Preliminary analyses with different assumptions about the evolutionary process revealed miniscule differences in the outcome. We therefore present the results of the model with the assumption of an Ornstein-Uhlenbeck process (*40*).

Mitogenome sequences for all 24 species (Table S1) were obtained from GenBank database (https://www.ncbi.nlm.nih.gov). Multiple sequence alignments were performed with CLUSTAL O v.1.2.4 (*41*) applying default settings. The alignment was trimmed to a length of 15690 positions to remove regions of excessive gaps at the beginning and at the end of the alignment. The best fitting model of substitutions was the General Time Reversible (GTR) model (*42*) with a gamma shape distribution parameter $\alpha = 0.8012$ (5 categories) and a proportion of invariable sites of $I = 29.03\%$ (GTR+*G*+*I*). The model was determined using the model search function in MEGA X (*43*). The phylogenetic relationship among species was inferred by constructing a Maximum Likelihood (ML) tree in MEGA X implementing the GTR+*G*+*I* model. Support for nodes was estimated via bootstrapping based on 100 iterations using all positions.

General synthesis route for fluorescent cholic acid derivatives

NMR data for compound struture verification are provided (Table S5).

Cholic-Lys(Z)-OH (5)

Chemical Formula: $C_{38}H_{58}N_2O_8$
Exact Mass: 670.42
Molecular Weight: 670.89
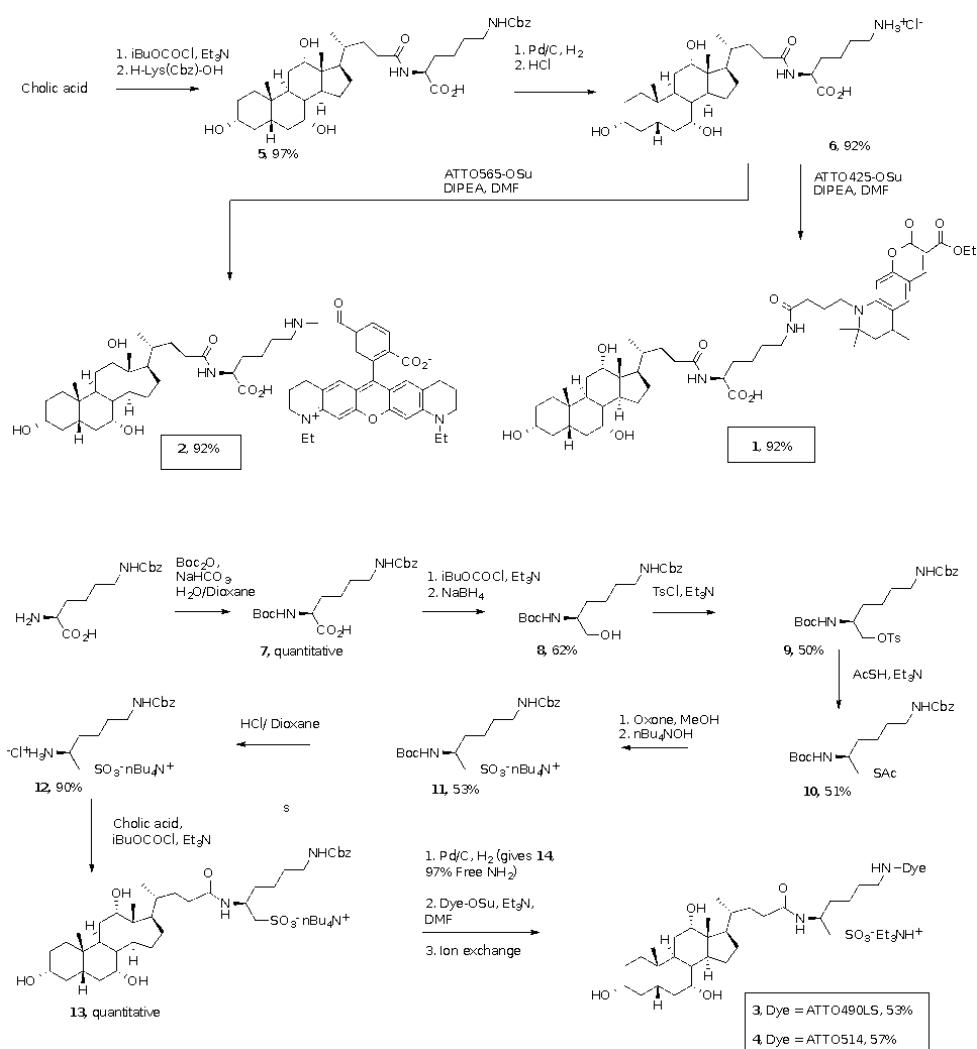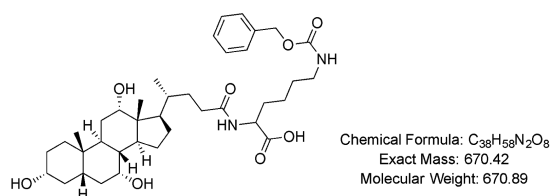
In a round bottom flask, cholic acid (2.0 g, 4.89 mmol) was dissolved in acetone (20 mL), triethylamine (1.4 equiv., 1.0 mL, 6.85 mmol) was added and the mixture was stirred for 20 min. After cooling to 0°C with an ice bath, ethyl chloroformate (0.46 mL, 4.89 mmol) was added dropwise and the mixture was allowed to stir for 90 min. In parallel, another round bottom flask was charged with a fresh solution of aqueous NaOH (0.5 M), H-Lys(Z)-OH (1.37 g, 4.89 mmol) was added and the reaction stirred for 60 min. The resulting mixture was transferred to the first flask and stirred overnight at room temperature. The pH of the mixture was adjusted to 2-2.5 with a 1M HCl solution and the compound was extracted with EtOAc. The organic layer was washed with water, dried over Na_2SO_4, filtered and concentrated to give compound **5** (3.20 g, 4.77 mmol) as a white solid, in 97% yield.

Rf: 0.28 CH_2Cl_2/MeOH (8:2)

^{1}H NMR (600 MHz, MeOD) δ 7.34 (d, J = 4.4 Hz, 4H), 7.29 (q, J = 4.3 Hz, 1H), 5.06 (s, 2H), 4.35 (dd, J = 9.2, 4.8 Hz, 1H), 3.95 (s, 1H), 3.79 (d, J = 3.2 Hz, 1H), 3.37 (t, J = 4.5 Hz, 1H), 3.12 (t, J = 6.9 Hz, 2H), 2.35 − 2.15 (m, 4H), 2.03 − 1.92 (m, 2H), 1.92 − 1.78 (m, 5H), 1.77 − 1.63 (m, 3H), 1.63 − 1.50 (m, 7H), 1.47 − 1.26 (m, 7H), 1.10 (qd, J = 12.0, 5.6 Hz, 1H), 1.03 (d, J = 6.6 Hz, 3H), 0.98 (td, J = 15.6, 14.2, 4.6 Hz, 1H), 0.91 (s, 3H), 0.71 (s, 3H).

^{13}C NMR (151 MHz, MeOD) δ 176.9, 175.6, 158.9, 138.4, 129.4, 128.9, 128.7, 79.5, 74.0, 72.9, 69.0, 67.3, 53.5, 48.1, 47.5, 43.2, 43.0, 41.5, 41.0, 40.5, 36.8, 36.5, 35.9, 33.8, 33.2, 32.2, 31.2, 30.4, 29.6, 28.7, 27.9, 24.2, 24.2, 23.2, 17.8, 13.0.

HR-MS (ESI+, m/z) calcd for $C_{38}H_{58}N_2O_8$ [(M + Na)$^+$] 693.4085, found 693.4069.

Cholic-Lys(NH$_3$$^+Cl^-$)-OH (6)

Chemical Formula: $C_{30}H_{53}ClN_2O_6$
Exact Mass: 572.36
Molecular Weight: 573.21
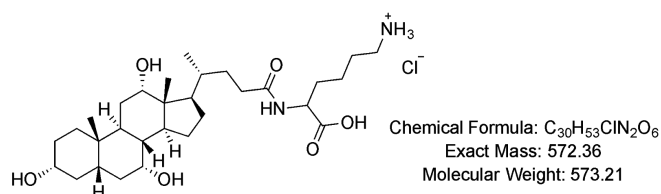
Cholic-Lys(Z) OH (**5**, 1.5 g, 2.24 mmol) was dissolved in EtOH (50 mL) and 10% of Pd/C was added. The solution was submitted to a hydrogen atmosphere overnight. After filtration through celite, the filtrate was evaporated to dryness. The product was then dissolved in water and the pH was adjusted to 2-2.5 with 1M HCl solution. The mixture was extracted with EtOAc and the aqueous layer was freeze-dried to obtain compound **6** as a white powder in quantitative yield.

^{1}H NMR (400 MHz, MeOD) δ 4.40 (dd, J = 9.2, 5.0 Hz, 1H), 3.98 (t, J = 4.0 Hz, 1H), 3.82 (q, J = 3.0 Hz, 1H), 3.46 – 3.38 (m, 1H), 2.96 (t, J = 7.7 Hz, 2H), 2.41 – 2.15 (m, 4H), 2.08 – 1.94 (m, 2H), 1.93 – 1.67 (m, 9H), 1.65 – 1.26 (m, 14H), 1.06 (d, J = 6.4 Hz, 3H), 1.03 – 0.97 (m, 1H), 0.94 (s, 3H), 0.74 (s, 3H).

^{13}C NMR (100 MHz, MeOD) δ 177.1, 174.1, 74.0, 72.8, 69.0, 53.5, 48.0, 47.5, 43.2, 43.0, 41.0, 40.5, 40.4, 36.9, 36.5, 35.9, 33.6, 33.1, 31.9, 31.2, 29.6, 28.7, 28.0, 27.9, 24.2, 23.9, 23.1, 17.8, 13.0.

HR-MS (ESI+, m/z) calcd for $C_{30}H_{52}N_2O_3$ [(M + H)$^+$] 537.3898, found 537.3881.

Cholic-Lys(ATTO425)-OH (1)

Chemical Formula: C52H77N3O11
Exact Mass: 919.56
Molecular Weight: 920.20
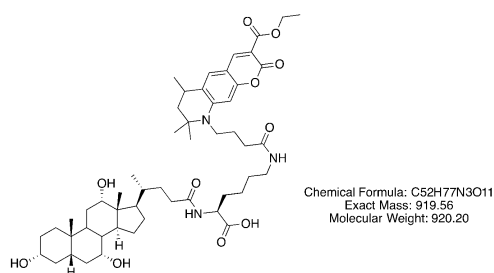
The amino compound MR15 (5.90 mg, 0.01 mmol) was dissolved in anhydrous DMF (0.4 mL), DIPEA (2.0 equiv., 3.70 x10^{-3} mL, 0.02 mmol) was added to adjust the pH around 8-9 followed by the addition of the succinimide ester of the fluorescent dye ATTO425 (1.0 equiv., 5.00 mg, 0.01 mmol). The mixture was stirred overnight in the dark and under argon atmosphere. The reaction was followed by LCMS, 0.5 equivalent of compound MR15 and DIPEA were added until complete consumption of the fluorescent dye. The reaction was complete after addition of 1.7 equivalent. The mixture was concentrated and purified by silica

column chromatography eluted with 30% of EtOAc/MeOH/AcOH/H_2O (3:3:3:2) in EtOAc. Compound **1** (8.50 mg, 9.24 x10^{-3} mmol) was obtained as a yellow powder in 92% yield.

^{1}H NMR (600 MHz, MeOD) δ 8.57 (s, 1H), 7.42 (s, 1H), 6.49 (s, 1H), 4.32 (q, J = 7.1 Hz, 2H), 4.29 (d, J = 6.8 Hz, 1H), 3.93 (t, J = 6.0 Hz, 1H), 3.76 (t, J = 2.9 Hz, 1H), 3.59 – 3.51 (m, 1H), 3.39 – 3.33 (m, 1H), 3.22 (t, J = 6.8 Hz, 2H), 2.89 (td, J = 9.3, 6.5, 3.6 Hz, 1H), 2.30 (m, 3H), 2.27 – 2.23 (m, 1H), 2.15 (td, J = 13.7, 11.3, 6.6 Hz, 1H), 2.00 – 1.82 (m, 9H), 1.82 – 1.76 (m, 2H), 1.75 – 1.62 (m, 3H), 1.61 – 1.47 (m, 9H), 1.43 (s, 3H), 1.38 (q, J = 6.8 Hz, 10H), 1.31 (s, 7H), 1.06 (dq, J = 12.2, 6.6, 6.2 Hz, 1H), 1.01 (d, J = 6.4 Hz, 3H), 0.89 (s, 3H), 0.66 (d, J = 1.8 Hz, 3H).

^{13}C NMR (151 MHz, MeOD) δ 176.1, 175.0, 165.7, 158.5, 153.2, 151.0, 128.7, 128.0, 109.1, 108.1, 97.8, 74.0, 72.9, 69.0, 62.1, 57.7, 55.5, 48.1, 47.5, 46.8, 46.0, 43.2, 43.0, 41.0, 40.5, 40.4, 36.9, 36.5, 35.9, 35.9, 34.4, 33.9, 33.5, 33.3, 31.2, 30.1, 29.7, 29.6, 28.7, 28.0, 27.9, 26.1, 25.3, 24.3, 24.2, 23.2, 19.9, 17.8, 14.6, 13.1.

HR-MS (ESI+, m/z) calcd for $C_{52}H_{77}N_3O_{11}$ [(M + Na)$^+$] 942.5450, found 942.5435.

Cholic-Lys(ATTO565)-OH (2)

Chemical Formula: $C_{61}H_{80}ClN_4O_{14}^-$
Exact Mass: 1127.54
Molecular Weight: 1128.78
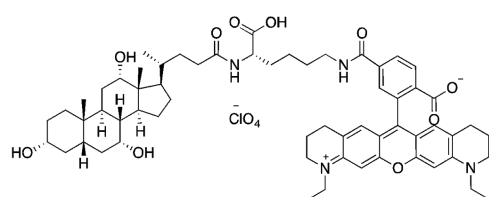
The amino compound **6** (1.8 equiv., 6.80 mg, 0.01 mmol) was dissolved in anhydrous DMF (0.4 mL), DIPEA (4 equiv., 3.00 x10^{-3} mL, 0.03 mmol) was added to adjust the pH around 8-9 followed by the addition of the succinimide ester of the fluorescent dye ATTO565 (1.0 equiv., 5.00 mg, 7.00 x10^{-3} mmol). The mixture was stirred overnight in the dark and under argon atmosphere. The reaction was followed by LCMS, 1 equivalent of compound **6** and DIPEA were added until complete consumption of the fluorescent dye. The reaction was

complete after addition of 3 equivalents. The mixture was concentrated and purified by silica column chromatography eluted with 30% of EtOAc/MeOH/AcOH/H_2O (3:3:3:2) in EtOAc. Compound **2** (7.30 mg, 6.47×10^{-3} mmol) was obtained as a pink powder in 92% yield.

^{1}H NMR (600 MHz, MeOD) δ 8.14 (d, J = 8.1 Hz, 1H), 8.10 – 8.05 (d, J = 8.0 Hz 1H), 7.68 (d, J = 1.7 Hz, 1H), 6.89 (d, J = 6.3 Hz, 4H), 4.26 (bs, 1H), 3.92 (s, 1H), 3.77 (d, J = 3.3 Hz, 1H), 3.66 (dt, J = 17.0, 7.1 Hz, 4H), 3.57 (t, J = 5.9 Hz, 4H), 3.42 – 3.36 (m, 3H), 2.71 (d, J = 6.4 Hz, 4H), 2.34 – 2.21 (m, 3H), 1.94 (m, 7H), 1.88 – 1.83 (m, 2H), 1.79 (m, 2H), 1.71 (m, 2H), 1.68 – 1.62 (m, 2H), 1.60 (m, 2H), 1.54 – 1.48 (m, 2H), 1.43 (m, 4H), 1.33 (m, 12H), 1.12 – 1.03 (m, 1H), 1.00 (d, J = 6.3 Hz, 3H), 0.96 (dd, J = 14.4, 3.4 Hz, 1H), 0.90 (s, 3H), 0.68 (s, 3H).

^{13}C NMR (151 MHz, MeOD) δ 176.1, 168.7, 160.1, 158.5, 154.7, 144.3, 136.5, 133.9, 131.1, 129.6, 129.2, 126.4, 126.4, 115.0, 95.7, 79.5, 74.0, 72.9, 69.0, 58.3, 55.8, 50.4, 49.8, 48.1, 47.8, 47.5, 43.2, 43.0, 41.1, 41.0, 40.5, 36.9, 36.5, 35.9, 35.9, 34.3, 33.5, 33.3, 31.2, 30.1, 29.6, 28.8, 28.5, 27.9, 24.4, 24.2, 23.2, 22.8, 22.1, 18.4, 17.8, 13.1, 11.3.

HR-MS (ESI+, m/z) calcd for $C_{61}H_{81}N_4O_{10}$ [(M + H)$^+$] 1030.6020, found 1030.6017.

Taurin Lysine

Boc-Lys(Z)-OH (7)
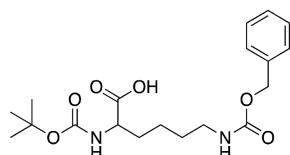
Chemical Formula: $C_{19}H_{28}N_2O_6$
Exact Mass: 380.19
Molecular Weight: 380.44

H-Lys(Z)-H (2.00 g, 7.13 mmol) was dissolved in 30 mL of H_2O and $NaHCO_3$ (3 equiv., 1.80 g, 21.40 mmol) was added. The mixture was cooled to 0°C before to add Boc_2O (1.5 equiv., 2.30 g, 10.70 mmol) and cold 1,4-dioxane (90 mL). The reaction was stirred overnight and evaporated to dryness to give compound **7** in 99% yield (2.70 g, 7.10 mmol).

^{1}H NMR (400 MHz, DMSO) δ 7.42 – 7.29 (m, 5H), 7.24 (t, J = 5.8 Hz, 1H), 7.02 (d, J = 8.0 Hz, 1H), 5.01 (s, 2H), 3.83 (td, J = 8.5, 7.9, 4.6 Hz, 1H), 2.98 (q, J = 6.5 Hz, 2H), 1.70 – 1.49 (m, 2H), 1.38 (s, 9H), 1.37 – 1.23 (m, 4H).

^{13}C NMR (100 MHz, DMSO) δ 174.3, 156.1, 155.6, 137.3, 128.4, 127.7, 79.2, 78.0, 65.1, 53.5, 30.4, 29.0, 28.2, 22.9.

Boc-Lys(Z)-CH₂OH (8)

Chemical Formula: $C_{19}H_{30}N_2O_5$
Exact Mass: 366.22
Molecular Weight: 366.46
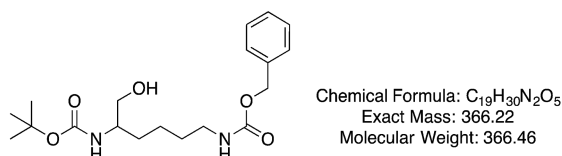
Boc-Lys(Z)-OH (**7**, 0.70 g, 1.80 mmol) and Et_3N (1.1 equiv., 0.28 mL, 2.00 mmol) were dissolved in anhydrous DMF (10 mL), the mixture was cooled to -10°C and ethylchloroformate (1.1 equiv., 0.19 mL, 2.00 mmol) was added dropwise. The reaction stirred for 30 min under argon atmosphere, filtered and rinsed with THF (3x). The filtrate was cooled to 0°C, $NaBH_4$ (3 equiv., 0.23 g, 6.00 mmol) was added as well as 70 mL of MeOH and the reaction was stirred for 1 h. The mixture was carefully quenched with HCl 2N and concentrated. After addition of H_2O, the product was extracted with EtOAc and the organic layer washed with HCl 1N, H_2O, sat. $NaHCO_3$ and brine (2x), dried over Na_2SO_4, filtered and concentrated. Purification on silica column chromatography eluted with Petrol/EtOAc (2:8) gave compound **8** (0.88 g, 2.39 mmol) in 62% yield.

Rf: 0.37 EtOAc/PET (8:2)

^{1}H NMR (400 MHz, MeOD) δ 7.34 (d, J = 4.3 Hz, 4H), 7.29 (dt, J = 9.1, 4.2 Hz, 1H), 5.06 (s, 2H), 3.55 – 3.38 (m, 3H), 3.12 (t, J = 6.8 Hz, 2H), 1.63 – 1.43 (m, 4H), 1.43 (s, 9H), 1.36 (m, 2H).

^{13}C NMR (100 MHz, MeOD) δ 158.8, 158.2, 138.3, 129.4, 128.9, 128.7, 79.9, 79.4, 67.2, 65.3, 53.6, 41.6, 31.9, 30.7, 28.8, 24.2.

HR-MS (ESI+, m/z) calcd for $C_{19}H_{30}N_2O_5$ [(M + Na)$^+$] 389.2047, found 349.2051.

Boc-Lys(Z)-CH₂OTs (9)

Chemical Formula: $C_{26}H_{36}N_2O_7S$
Exact Mass: 520.22
Molecular Weight: 520.64
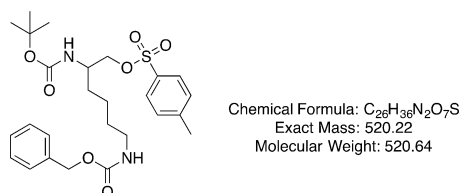
Boc-Lys(Z)-CH₂OH (**8**, 1.80 g, 4.93 mmol) was dissolved in 10 mL of anhydrous CH_2Cl_2, cooled to 0°C and TsCl (1.5 equiv., 1.40 g, 7.40 mmol) was added followed by Et_3N (2 equiv., 1.40 mL, 9.80 mmol). The reaction was stirred overnight, poured into H_2O and extracted with CH_2Cl_2. The product was dried over Na_2SO_4, filtered, concentrated and purified by silica column chromatography eluted with $CHCl_3$. Compound **9** (1.28 g, 2.40 mmol) was obtained in 50% yield.

^{1}H NMR (400 MHz, CDCl₃) δ 7.78 (d, *J* = 8.2 Hz, 2H), 7.43 − 7.27 (m, 7H), 5.09 (s, 2H), 4.76 (s, 1H), 4.62 (s, 1H), 4.10 − 3.92 (m, 2H), 3.72 (m, 0H), 3.15 (s, 2H), 2.45 (s, 3H), 1.39 (s, 15H).

^{13}C NMR (100 MHz, MeOD) δ 158.9, 157.9, 146.5, 138.4, 134.2, 131.1, 129.4, 129.1, 128.9, 128.8, 80.2, 79.5, 72.7, 67.3, 52.5, 41.5, 31.3, 30.5, 28.7, 24.0, 21.6.

HR-MS (ESI+, m/z) calcd for $C_{26}H_{36}N_2O_7S$ [(M + Na)$^+$] 543.2135, found 543.2112.

Boc-Lys(Z)-CH₂SCOCH₃ (10)

Chemical Formula: $C_{21}H_{32}N_2O_5S$
Exact Mass: 424.20
Molecular Weight: 424.56
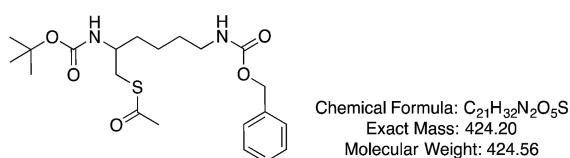
Compound **9** (0.23 g, 0.44 mmol) was dissolved in CHCl₃ (5 mL) and DIPEA (5 equiv., 0.38 mL, 2.21 mmol) was added followed by thioacetic acid (5 equiv., 0.16 mL, 2.21 mmol)

dissolved in 1 mL of $CHCl_3$. The mixture was stirred overnight under argon atmosphere and followed by LCMS. 3 equivalents of thioacetic acid and DIPEA were added every day and the reaction was complete the third day. The mixture was washed with brine, extracted with $CHCl_3$, dried over Na_2SO_4, filtered and concentrated. The residual solid was dissolved in CH_2Cl_2 and treated with active charcoal overnight. After filtration and purification on silica column chromatography eluted with $CHCl_3$, compound **10** (0.10 g, 0.23 mmol) was obtained in 51% yield.

Rf: 0.60 $CHCl_3$/MeOH (95:5)

^{1}H NMR (400 MHz, Chloroform-*d*) δ 7.26 – 7.15 (m, 5H), 4.96 (s, 2H), 4.69 (s, 1H), 4.38 (s, 1H), 3.59 (s, 1H), 3.05 (q, *J* = 6.8 Hz, 2H), 2.98 – 2.78 (m, 2H), 2.21 (s, 3H), 1.47 – 1.31 (m, 4H), 1.28 (s, 9H), 1.26 – 1.17 (m, 2H).

^{13}C NMR (100 MHz, $CDCl_3$) δ 195.7, 156.5, 155.6, 136.6, 128.5, 128.1, 128.1, 79.4, 66.6, 50.3, 40.7, 33.9, 30.6, 29.5, 28.4, 23.0.

HR-MS (ESI+, m/z) calcd for $C_{21}H_{32}N_2O_5S$ [(M + Na)$^+$] 447.1924, found 447.1919.

Boc-Lys(Z)-$CH_2SO_3^-nBu_4^+$ (11)

Chemical Formula: $C_{35}H_{65}N_3O_7S$
Exact Mass: 671.45
Molecular Weight: 671.98
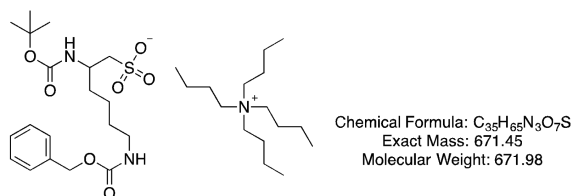
Compound **10** (0.10 g, 0.23 mmol) was dissolved in MeOH (5 mL) and a solution of oxone (3.5 equiv., 0.25 g, 0.80 mmol) in 5 mL of H_2O was added. The mixture was stirred for 1.5 h, tetrabutylammonium hydroxide solution 40 wt. % in H_2O (0.34 mL) in 2mL of H_2O was added and the stirring was continued for 16 h. The methanol was concentrated under vacuum, the compound diluted with H_2O and extracted with CH_2Cl_2, dried over Na_2SO_4, filtered and concentrated. Purification by silica column chromatography and elution with $CHCl_3$ gave

47

compound **11** (0.08 g, 0.12 mmol) in 53% yield.

Rf: 0.24 CHCl$_3$/MeOH (9:1)

^{1}H NMR (600 MHz, Chloroform-*d*) δ 7.36 − 7.32 (m, 4H), 7.32 − 7.27 (m, 1H), 5.14 − 4.99 (m, 2H), 3.91 − 3.83 (m, 1H), 3.28 − 3.25 (m, 8H), 3.24 − 3.11 (m, 2H), 3.04 (ddd, *J* = 58.4, 14.2, 4.5 Hz, 2H), 1.65 − 1.61 (m, 8H), 1.58 − 1.47 (m, 2H), 1.43 (q, *J* = 7.3 Hz, 10H), 1.39 (s, 11H), 1.00 (t, *J* = 7.3 Hz, 6H).

^{13}C NMR (151 MHz, CDCl$_3$) δ 156.7, 156.0, 137.2, 128.5, 128.1, 128.0, 78.5, 66.4, 59.0, 53.6, 48.1, 40.4, 32.8, 29.1, 28.6, 24.2, 23.0, 19.9, 13.8.

HR-MS (ESI+, m/z) calcd for C$_{19}$H$_{30}$N$_2$O$_7$S [(M + H)$^+$] 431.1846, found 431.1839.

Cl⁻NH$_3^+$-Lys(Z)-CH$_2$SO$_3^-$nBu$_4^+$ (12)

Chemical Formula: C$_{30}$H$_{58}$ClN$_3$O$_5$S
Exact Mass: 607.38
Molecular Weight: 608.32
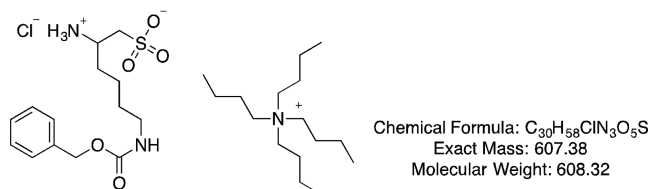
At 0°C, compound **11** was dissolved in 4M HCl/dioxane solution and the mixture was stirred for 2 h at rt. Evaporation to dryness gave the chloride salt **12** (0.06 mg, 0.11 mmol) in 90% yield.

^{1}H NMR (400 MHz, Deuterium Oxide) δ 6.99 (m, 5H), 4.67 (s, 2H), 3.25 − 3.19 (m, 1H), 2.79 − 2.72 (m, 8H), 2.70 (s, 4H), 1.32 (q, *J* = 7.6 Hz, 2H), 1.20 (p, *J* = 7.8 Hz, 8H), 1.08 (q, *J* = 7.0 Hz, 2H), 0.91 (q, *J* = 7.4 Hz, 10H), 0.50 (t, *J* = 7.4 Hz, 12H).

^{13}C NMR (151 MHz, MeOD) δ 159.0, 138.4, 129.5, 129.0, 128.8, 67.4, 59.5, 59.5, 59.5, 52.8, 50.3, 41.2, 33.3, 30.4, 24.8, 23.2, 20.7, 20.7, 20.7, 13.9.

HR-MS (ESI+, m/z) calcd for $C_{14}H_{22}N_2O_5S$ [(M + H)$^+$] 331.1322, found 331.1303.

Chol-Lys(Z)-CH$_2$SO$_3^-$nBu$_4^+$ (13)

Chemical Formula: $C_{54}H_{95}N_3O_9S$
Exact Mass: 961.68
Molecular Weight: 962.43
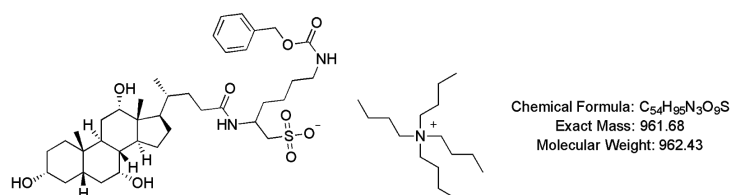
In a round bottom flask, cholic acid (21 mg, 0.05 mmol) was dissolved in acetone (0.6 mL), Et$_3$N (1.4 equiv., 0.01 mL, 0.07 mmol) was added and the mixture was stirred for 10 min. After cooling to 0°C with an ice bath, ethyl chloroformate (5.0×10^{-3} mL, 0.05 mmol) was added dropwise and the mixture was allowed to stir for 90 min. In parallel, another round bottom flask was charged with a fresh solution of 0.5 M NaOH (1 mL), compound **12** (0.03 g, 0.05 mmol) was added and the reaction stirred for 60 min. The resulting mixture was transferred to flask (1) and stirred overnight at rt. After concentration to dryness, compound **13** (0.05 g, 0.05 mmol) occurred as a white solid in quantitative yield.

^{1}H NMR (600 MHz, Methanol-d_4) δ 7.41 – 7.25 (m, 5H), 5.06 (s, 2H), 4.26 (dq, J = 11.0, 5.6 Hz, 1H), 3.95 (dt, J = 6.3, 3.0 Hz, 1H), 3.79 (p, J = 3.0 Hz, 1H), 3.38 (m, 1H), 3.26 – 3.23 (m, 8H), 3.11 (t, J = 6.9 Hz, 2H), 3.03 – 2.90 (m, 3H), 2.33 – 2.21 (m, 4H), 2.10 (m, 1H), 2.01 – 1.93 (m, 2H), 1.90 – 1.85 (m, 2H), 1.83 – 1.79 (m, 2H), 1.74 (dd, J = 6.4, 3.7 Hz, 1H), 1.66 (m, 9H), 1.59 – 1.52 (m, 8H), 1.42 (m, 10H), 1.35 – 1.31 (m, 2H), 1.24 – 1.22 (m, 2H), 1.10 (m, 1H), 1.04 – 1.01 (m, 15H), 0.98 (m, 1H), 0.91 (s, 3H), 0.70 (s, 3H).

^{13}C NMR (151 MHz, MeOD) δ 183.5, 176.0, 158.9, 138.5, 129.4, 128.9, 128.7, 74.0, 72.9, 69.0, 67.2, 59.5, 56.0, 48.1, 47.7, 47.5, 43.2, 43.0, 41.6, 41.0, 40.5, 36.9, 36.5, 35.9, 34.4, 33.3, 31.2, 30.5, 29.6, 28.7, 27.9, 24.8, 24.2, 24.1, 23.2, 20.7, 17.8, 14.0, 13.0.

HR-MS (ESI+, m/z) calcd for $C_{38}H_{60}N_2O_9S$ [(M + Na)$^+$] 743.3912, found 743.3913.

Chol-Lys(NH₂)-CH₂SO₃⁻nBu₄⁺ (14)

Chemical Formula: $C_{46}H_{89}N_3O_7S$
Exact Mass: 827.64
Molecular Weight: 828.29
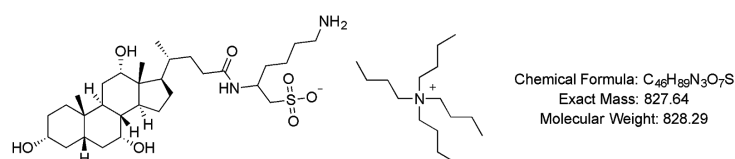
Compound **13** (0.05 g, 0.05 mmol) was dissolved in EtOH/THF (1:1, 5 ml), 10% of Pd/C (0.05 g) was added and the mixture submitted to a hydrogen atmosphere overnight. After filtration through celite and rinsing with EtOH, the compound was freeze-dried and **14** was obtained as a yellowish solid in 97% yield.

^{1}H NMR (600 MHz, Methanol-d_4) δ 4.29 (s, 1H), 3.95 (s, 1H), 3.79 (s, 1H), 3.41 – 3.34 (m, 1H), 3.26 – 3.21 (m, 5H), 3.08 – 2.99 (m, 2H), 2.93 (dd, J = 14.0, 7.1 Hz, 2H), 2.26 (m, 3H), 2.02 – 1.94 (m, 3H), 1.88 (d, J = 13.3 Hz, 3H), 1.83 – 1.78 (m, 2H), 1.69 – 1.64 (m, 7H), 1.57 (m, 5H), 1.44 – 1.39 (m, 9H), 1.33 – 1.23 (m, 4H), 1.14 – 1.08 (m, 1H), 1.04 – 1.00 (m, 12H), 0.99 – 0.96 (m, 1H), 0.92 (s, 3H), 0.71 (s, 3H).

^{13}C NMR (151 MHz, MeOD) δ 176.0, 74.0, 72.9, 69.0, 59.5, 55.6, 52.0, 44.0, 43.2, 43.0, 41.0, 40.5, 36.9, 36.7, 36.5, 35.9, 34.4, 32.2, 31.9, 31.2, 29.6, 28.7, 27.9, 24.8, 24.2, 23.5, 23.2, 20.7, 17.8, 13.9, 13.0.

Chol-Lys(ATTO490LS)-CH₂SO₃⁻nBu₄⁺ (3)
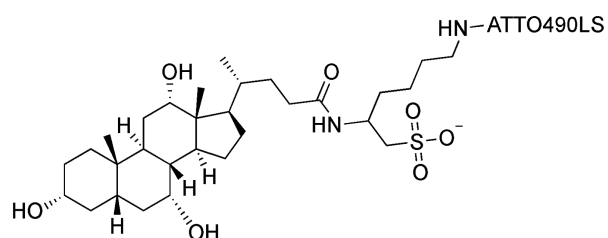
MW(nBu₄ salt) = 1484 g.mol^{-1}

MW(Et₃N salt) = 1344 g.mol^{-1}

M= 1242

Compound **14** (10.40 mg, 12.60 x10^{-3} mmol, 2 equiv.) was dissolved in 0.5 mL of dry DMF and DIPEA (2.20 μL, 12.60 x10^{-3} mmol, 2 equiv.) was added to the solution, the pH reached

50

Supplementary Figure Legends

Figure S1 A. Alternative geometry of activation does not influence spatial decay symmetry. In vivo time-lapse imaging of the decay of CMNB-Fluorescein from the canalicular network, following activation (white dotted line) in a stripe geometry. Graph shows the symmetric decay with no shift of the center of mass of the intensity (black line). Scale bar: 30 μm. **B. Area of photoactivation influences half-life of decay.** Graphs show the circular spatial activation profiles CMNB-Fluorescein of varying radius, with correspondingly varying half-life of temporal decay as predicted by the diffusion equation $t_{1/2}$ = r^2 / 4D. The individual colors indicate independent photoactivations using the same conditions.

Figure S2 A. Representative ICS imaging sequences taken of an IBD taken at various frame times showing animal movements in raw intensity. The temporal color coded project illustrates the deviations introduced. Scale bar: 10 μm. **B.** The graphs show the periodic variation of the temporal autocorrelation due to animal movements (black) and corresponding band-pass Fourier-filtered autocorrelation curves to remove these variations (red).

Figure S3 A. Calibration curve of CLF in mouse bile, indicating the non-linearity in lower concentration ranges, near-linearity in most of the concentration range up to 400 μM of CLF and detector saturation beyond 400 μM. The Boltzmann fit provides a convenient function for interconversion of concentrations and intensity values for CLF in bile. **B.** Photoactivation of CMNB-Fluorescein in vitro in water, mouse bile, bovine bile, or 1% albumin solution showing that diffusion of fluorescein can be significantly reduced by binding to hydrophobic

components (proteins, micelles, etc.) known to be present in bile. **C.** Time-lapse imaging (top) and temporal clearance of a poorly-exported bile salt analog CL-ATTO565(red) and a well-exported analog CL-ATTO405 (blue), showing a strong correlation between hepatocyte intensity and canalicular intensity over the time required for clearance. This indicates that hepatocyte export kinetics to the canaliculi is a major determinant of canalicular clearance, and that the canalicular excretion rate is not rate-limiting for overall clearance of the bile salt analogues. The table provides the Pearson correlation coefficients between hepatocyte intensity and canalicular intensity over time.

Figure S4: Maximum Likelihood tree displaying the relationships among 24 mammal species. The tree with the highest log likelihood (-185812.18) is shown and was constructed applying the GTR+*G*+*I* model. Bootstrap support values are displayed next to the branches as proportions. The tree is drawn to scale.

Table S1: Results and data for velocity and diffusion in liver microcompartments obtained from fluorescence loss after photoactivation

Diffusion coefficients and velocities calculated using the Soumpasis method (see Supplementary Information - Photo-activation) for single photoactivations performed in CV, PV, MZ and IBD zones of the liver, under treatment conditions corresponding to basal (control), secretin bolus or TCA-infusion. Each row represents an independent photoactivation sequence. Zero values in velocity columns indicate that no shift could be detected in the centroid of the photoactivated region over time. Cases where a half-life could not be determined as marked 'n.d' and were not used. These data are graphically represented in Fig. 2C.

Table S2: Results and data for diffusion in liver microcompartments obtained from spatial ICS.

Diffusion coefficients (D) derived from fitting of spatial autocorrelation decays in the y-direction (RICS-y) in CV, PV, MZ and IBD zones of the liver, under treatment conditions corresponding to basal (control), secretin bolus or TCA-infusion. The 'Region' column classifies the liver domains into canalicular or ductular zones. The 'w0' and 'wz' columns correspond to the beam waist and axial beam height used as fit parameters (see Supplementary Information - IVARICS). The 'COD : R^2' column provides the coefficient of determination of the non-linear global fit to a 1-population 3D-diffusion function, and the 'Bound encountered' column records if the bound was encountered during fitting iterations. Raw data files are referenced in the filename column and corresponding autocorrelation curves and fits are available (see Appendix). ICS data with fitting COD < 0.8 or in which the

fitting bound was encountered (marked red) were not used for further analysis. These data are graphically represented in Fig. 3E.

Table S3: **Results and data for diffusion and velocity in liver microcompartments obtained from temporal ICS.**

Diffusion coefficients (D) and advection velocities (V) derived from fitting of temporal autocorrelation decays in CV, PV, MZ and IBD zones of the liver, under treatment conditions corresponding to basal (control), secretin bolus or TCA-infusion. The 'Region' column classifies the liver domains into canalicular or ductular zones. The 'w0' and 'wz' columns correspond to the beam waist and axial beam height used as fit parameters (see Supplementary Information - IVARICS). The 'COD : R^2' column provides the coefficient of determination of the non-linear global fit for a 1-population diffusion and velocity function, and the 'Bound encountered' column records if the bound was encountered for either D or V during fitting iterations. Raw data files are referenced in the 'File' column and corresponding autocorrelation curves and fits are available (see Appendix). ICS data with fitting COD < 0.8 or in which the fitting bound was encountered (marked red) were not used for further analysis. These data are graphically represented in Fig. 3E.

Table S4: NMR spectra of custom synthesized cholic acid derivatives

NMR spectra of custom synthesized cholic acid derivatives (see Supplementary Information - General synthesis route for fluorescent cholic acid derivatives) are provided, showing peaks relevant to confirm the chemical structure of the synthesized compound.

Table S5: Results and data utilized for cross-species lobular analysis

Liver weight, body weight, lobule area, diameter of hepatocyte nuclei and density of nuclei of 24 mammalian species. One row per analysed individual (i.e. image). The columns give the english and latin names of the species, identification numbers (ID), antibody and its dilution used for glutamine synthetase immunostaining, mean and standard deviation (SD) of the body mass of the individual species in gram (g), the corresponding mean and SD of the liver mass, sources of body weight and liver weight, comments explaining the derivation of liver and body weight wherever necessary, number of analyzed lobules immunostained for glutamine synthetase (No. of lobules), mean value and SD of lobule area (mm 2), mean and SD of the nuclear diameter (μm), and nuclear density in the analyzed area (mm-2). Cases where a certain parameter could not be determined due to failure of the sample to meet quality control standards is marked as 'n.d.' for 'not determined'.

Supplementary Movies

Movie S1: Photoactivation of CMNB-Fluorescein in various domains of the liver biliary network**.**

Movie S2: Photoactivation of CMNB-Fluorescein in using stripe geometry in the liver canalicular network**.**

Movie S3: Photoactivation of CMNB-Fluorescein in various domains of the liver biliary network under basal, secretin- or TCA-stimulated conditions**.**

Movie S4: Photoactivation of CMNB-Fluorescein in 3D showing symmetric dispersion in the liver canalicular network.

Movie S5: Aliasing effects in RICS sequences due to animal movements and their representation in the spatial autocorrelation**.**

Movie S6: Clearance of CLF from the liver canalicular network under basal, secretin- or TCA-stimulated conditions**.**

Movie S7: Clearance of fluorescein in its native form with and without the presence of cholic acid, or as CLF (fluorescein conjugated with cholic acid).

Appendix

Compilation of raw spatial and temporal autocorrelation curves, and individual fits are provided.

Raw data files and analysis code are available at: https://lab.vartak.org/repository/bile-flux/
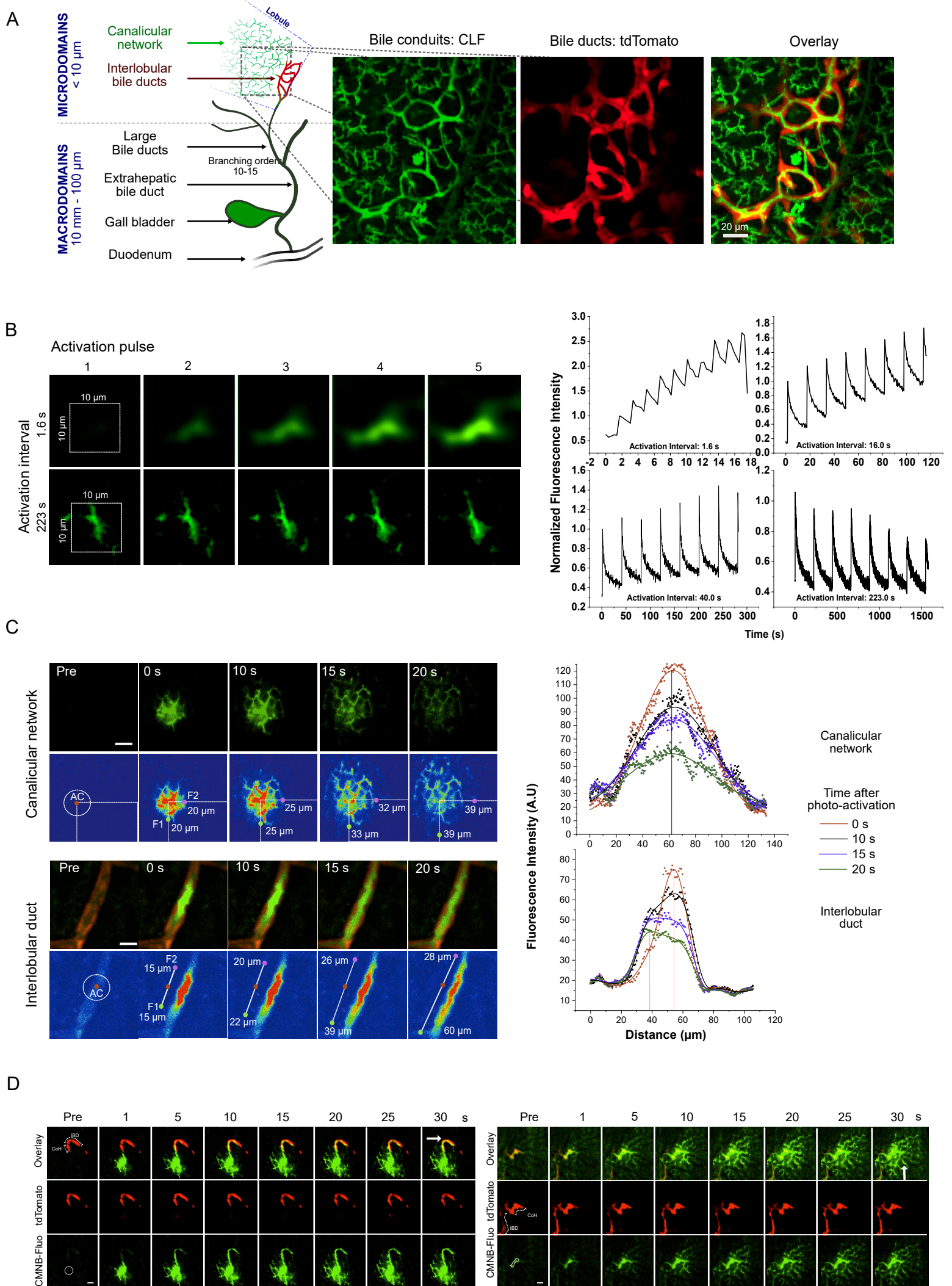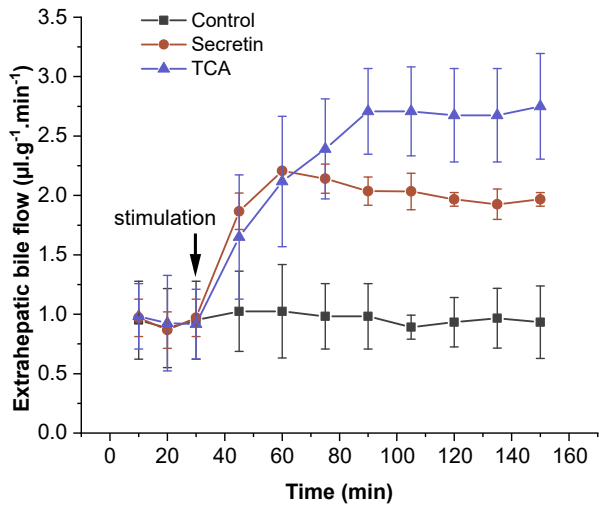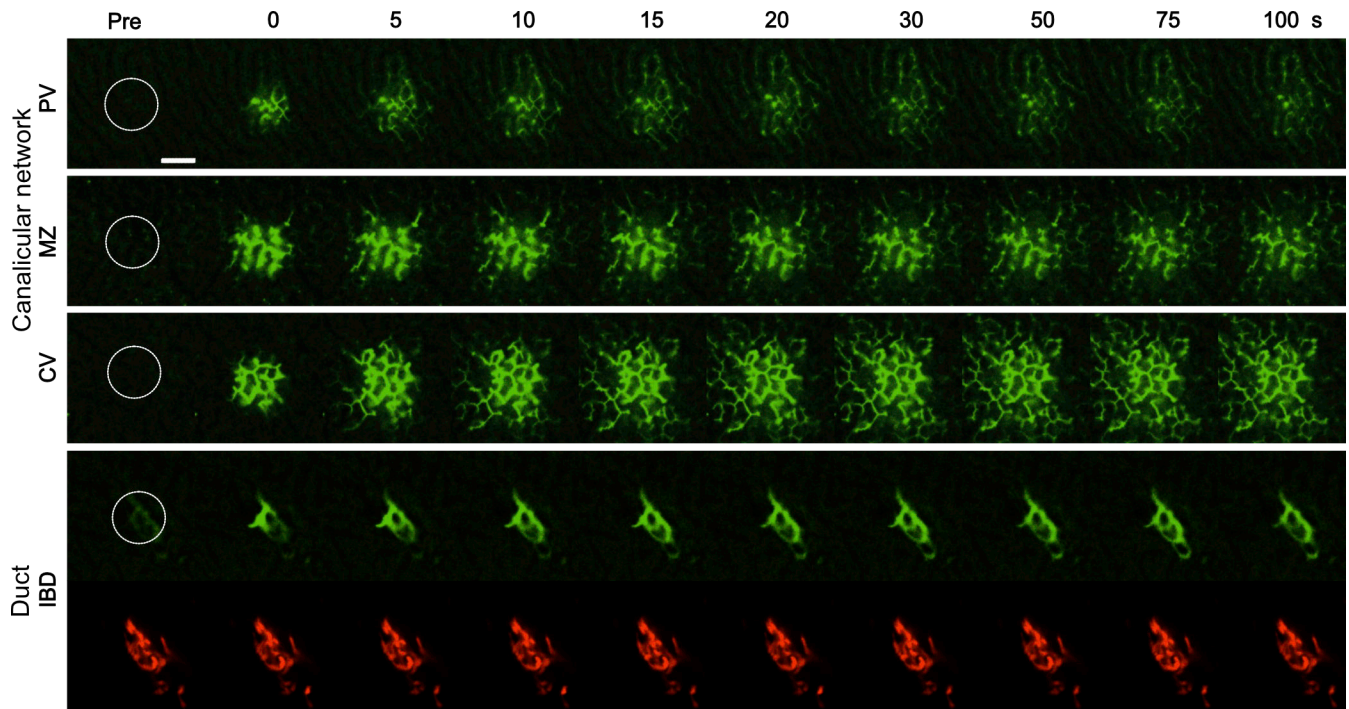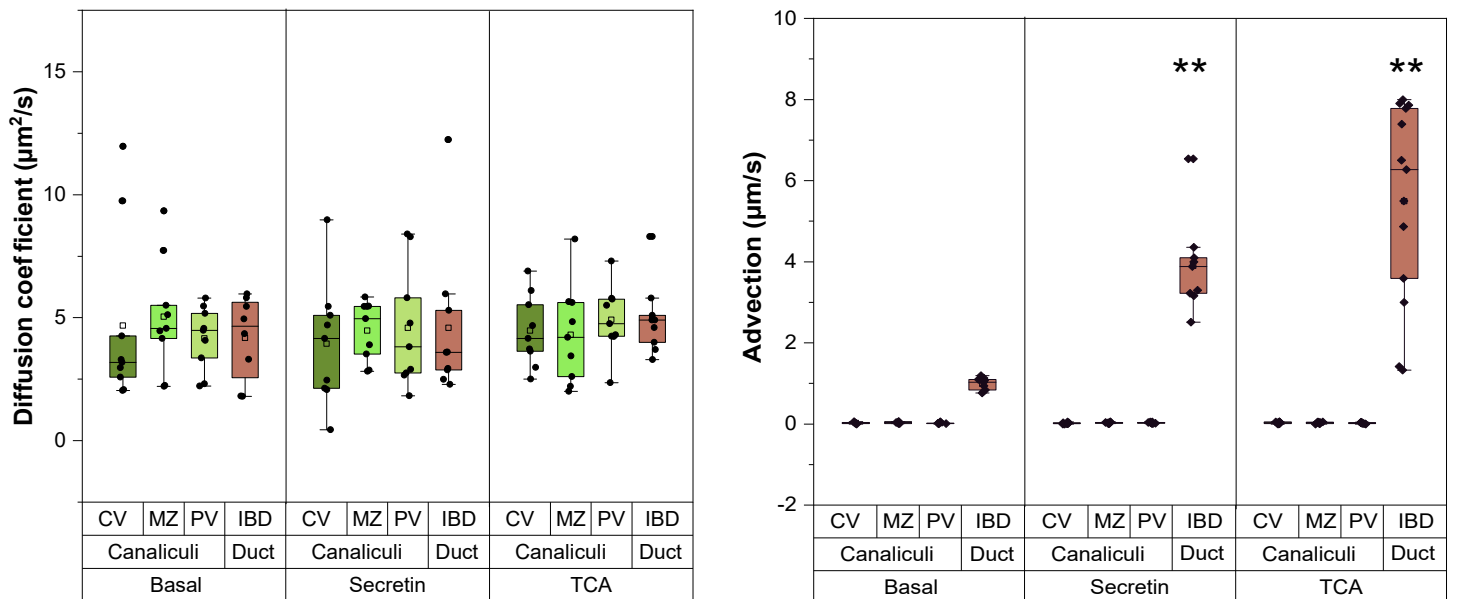
Figure 1

A — MICRODOMAINS < 10 µm / MACRODOMAINS 10 mm - 100 µm. Canalicular network, Interlobular bile ducts, Lobule, Large Bile ducts, Extrahepatic bile duct, Gall bladder, Duodenum, Branching order 10-15. Bile conduits: CLF; Bile ducts: tdTomato; Overlay. Scale bar 20 µm.

B — Activation pulse 1–5; Activation interval 1.6 s and 223 s; 10 µm scale. Normalized Fluorescence Intensity vs Time (s) for Activation Intervals: 1.6 s, 16.0 s, 40.0 s, 223.0 s.

C — Canalicular network and Interlobular duct: Pre, 0 s, 10 s, 15 s, 20 s. Fluorescence Intensity (A.U) vs Distance (µm). Time after photo-activation: 0 s, 10 s, 15 s, 20 s.

D — Overlay, tdTomato, CMNB-Fluo; Pre, 1, 5, 10, 15, 20, 25, 30 s.
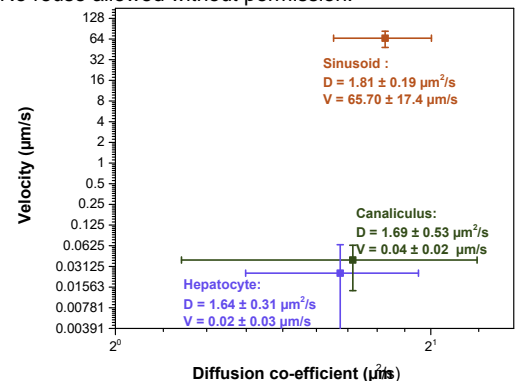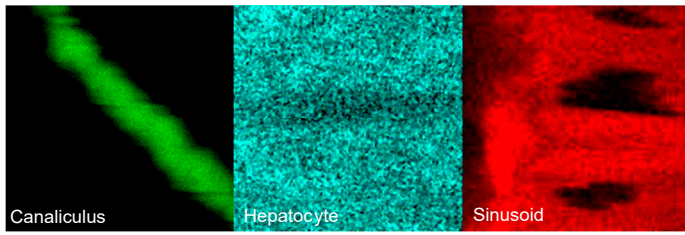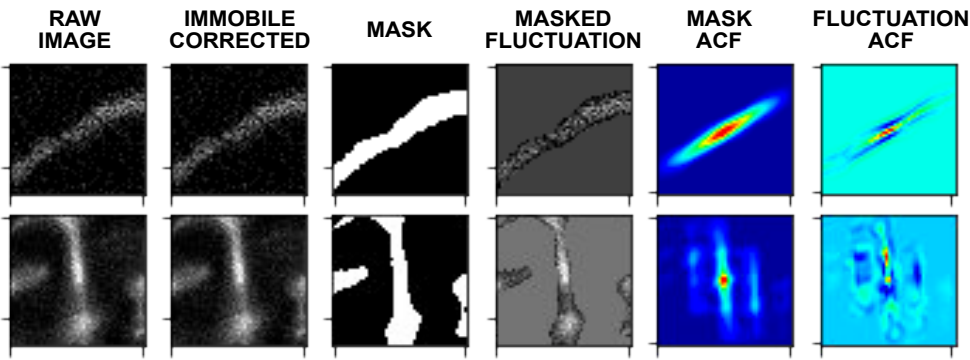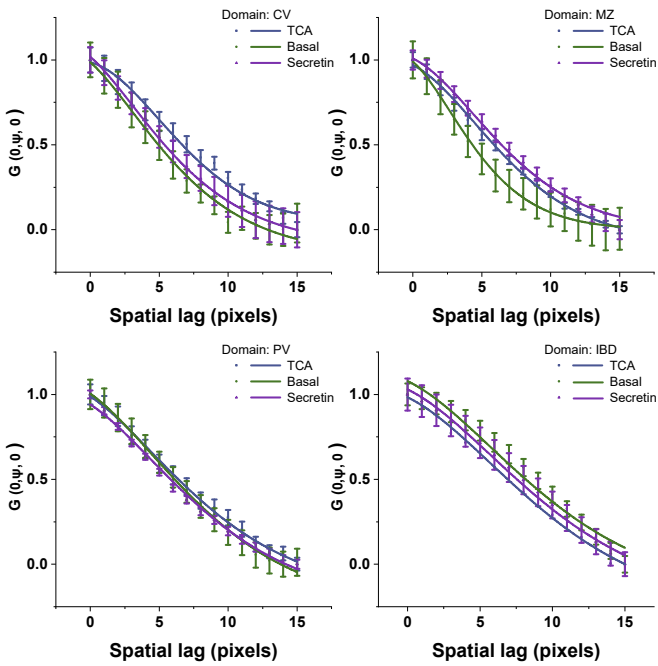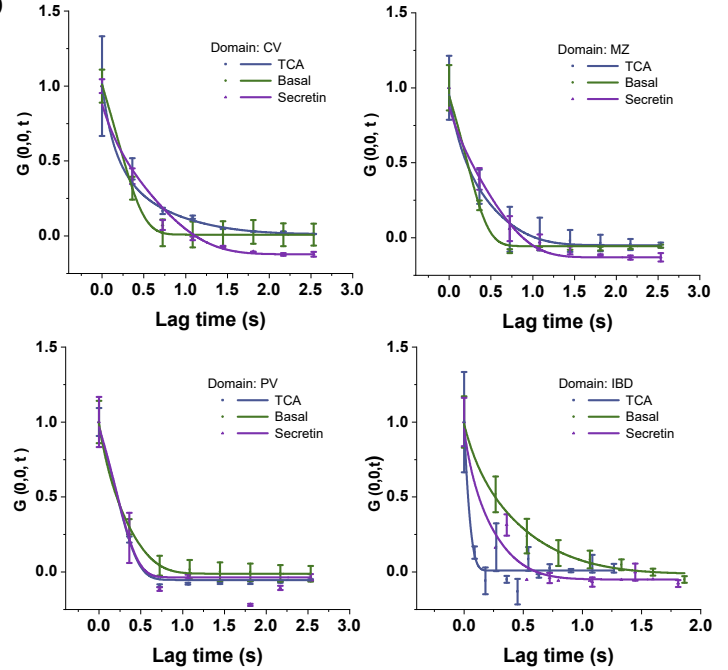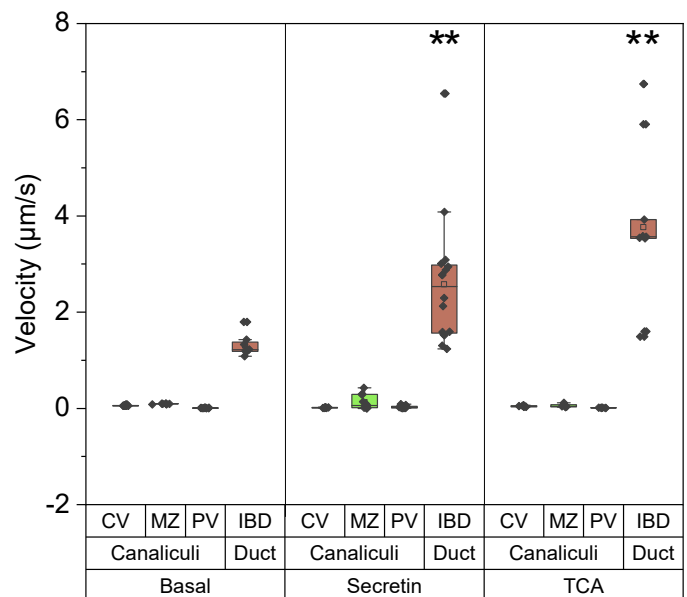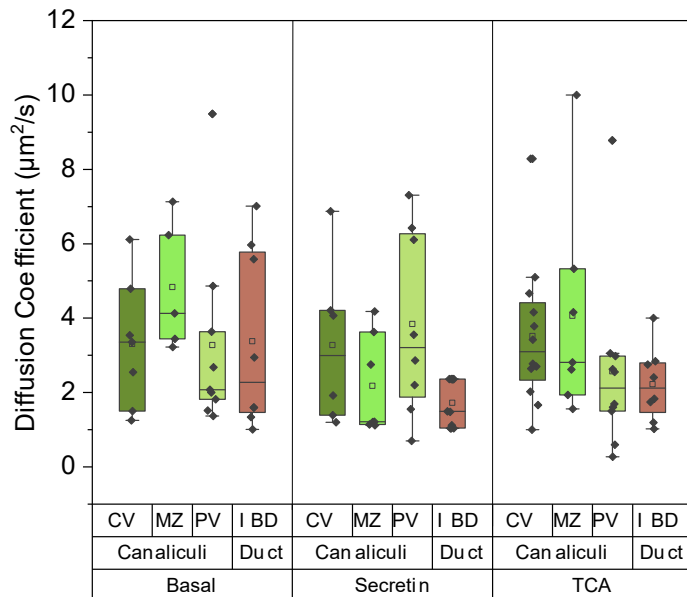
Figure 2

Figure 3

Figure 4

A

Confocal Z-stack:
Canaliculi (Anti-DPP4, green),
Duct (Anti-KRT19, magenta)

3D Wireframe representation of conduit lumina
(0.4 μm mesh)

B Activation pulse

Activation interval

1.6 s

223 s

Activation Interval: 1.6 s

Activation Interval: 16.0 s

Activation Interval: 40.0 s

Activation Interval: 223.0 s

Normalized intensity

Time (s)
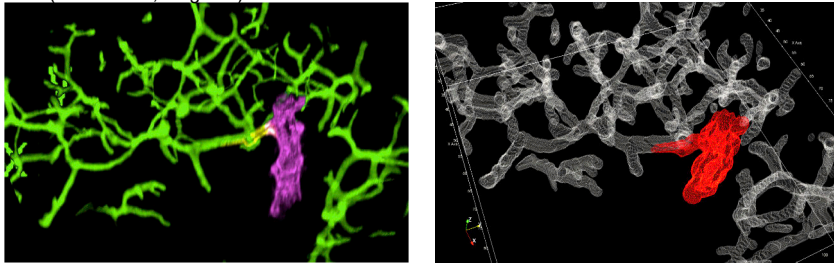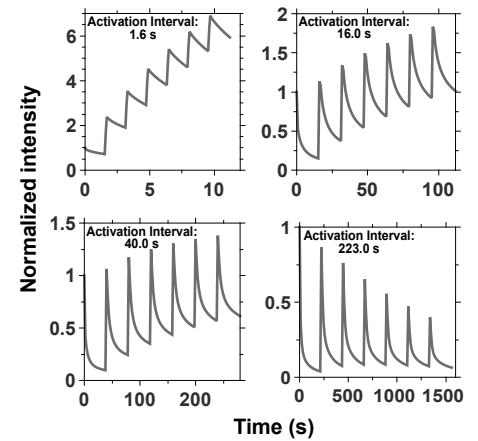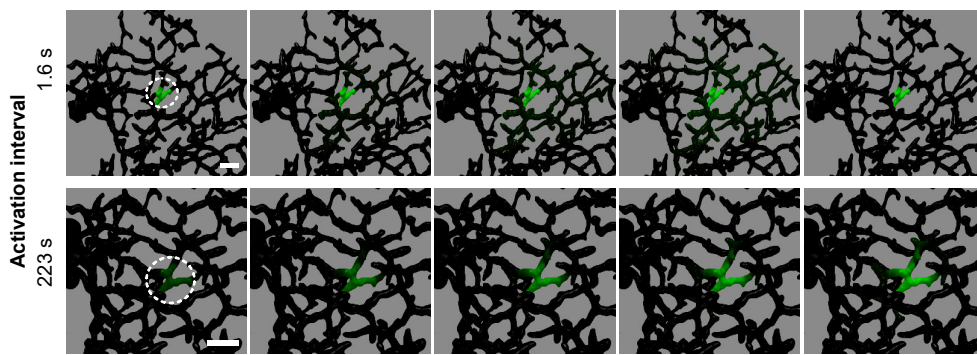
C **Canalicular network** Diffusion coefficient = 3 μm²/s
Advection velocity = 0 μm/s

r = 5 μm

r = 10 μm

Concentration

Time (s)
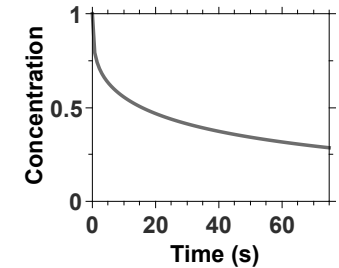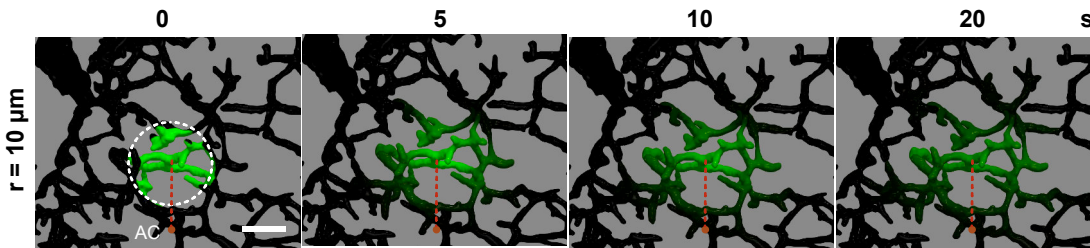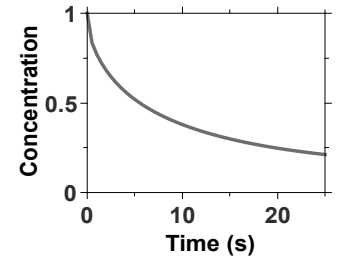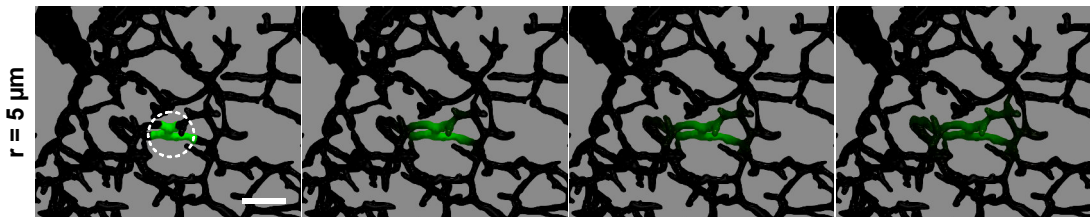
Interlobular duct Diffusion coefficient = 3 μm²/s
Advection velocity = 1 μm/s

r = 5 μm

**Spatial profile:
Interlobular duct**

t=0s
t=10s
t=15s
t=20s

Concentration

Distance (μm)

**Spatial profile:
Canalicular network**

t=0s
t=10s
t=15s
t=20s

Concentration

Distance (μm)
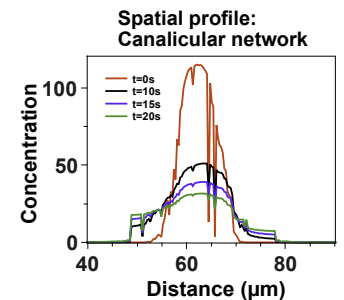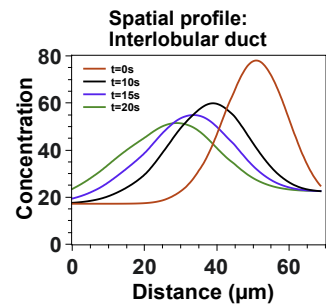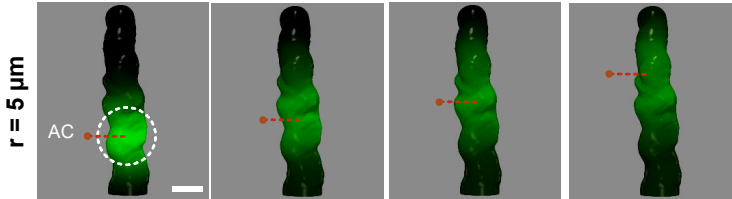
D **Canal of Hering** Diffusion coefficient = 3 μm²/s
Advection velocity = 1 μm/s

Figure 5

Figure 6

A

Automatic cross-species lobule analysis

Anti-glutamine synthetase histology (brown) + Hematoxylin counterstaining (blue)

↓

Central vein identification

↓

Watershed algorithm

↓

Lobular boundary identification (black)

↓

Prune for quality control (red)

↓

Quantification

B
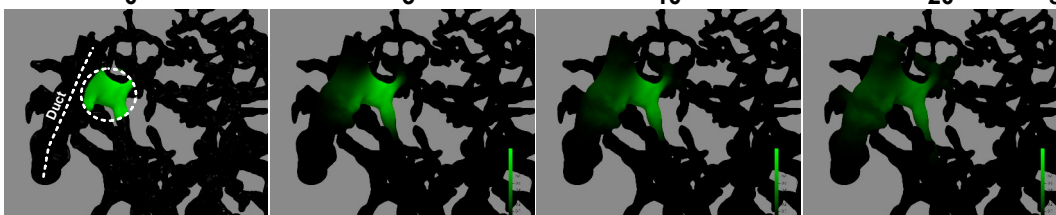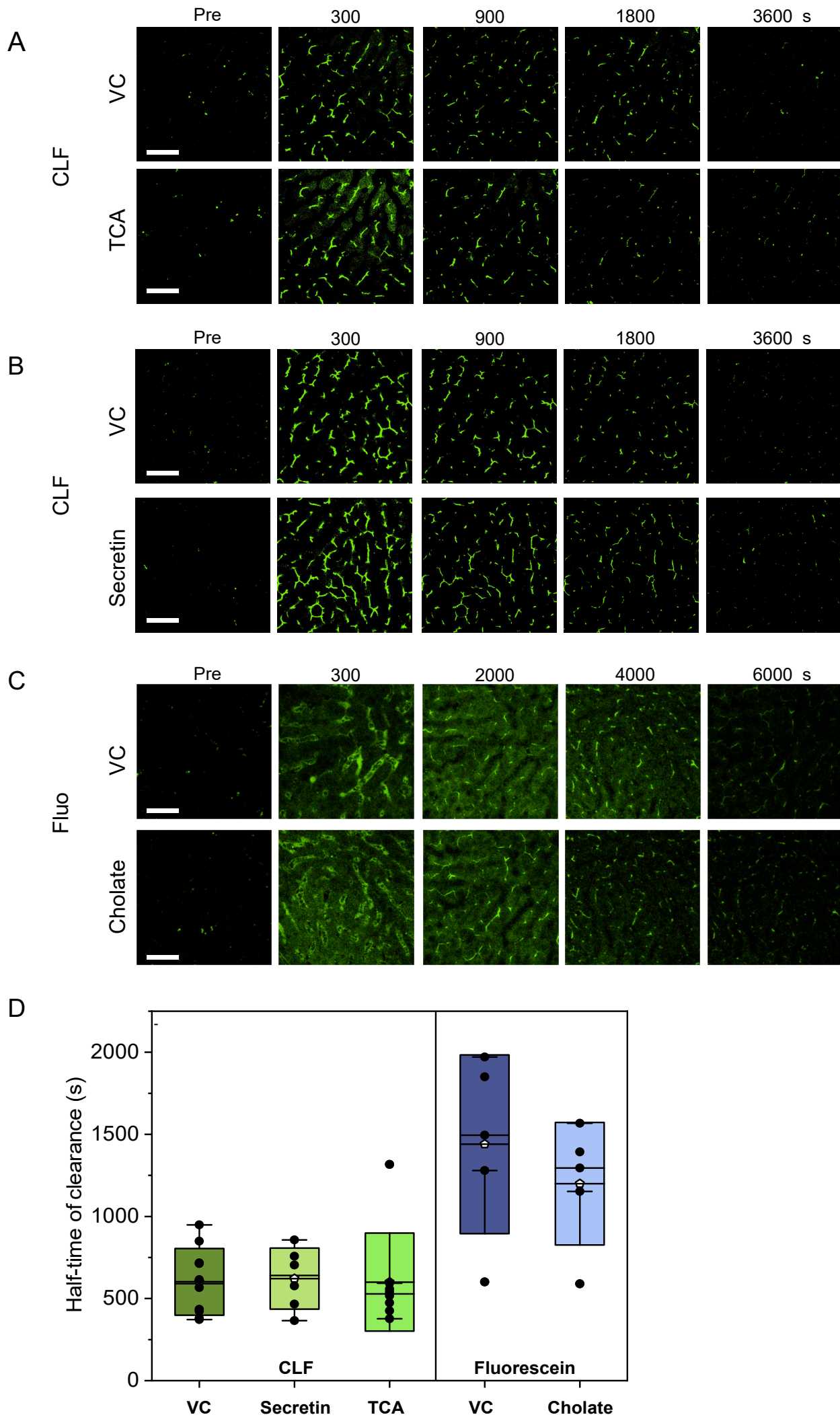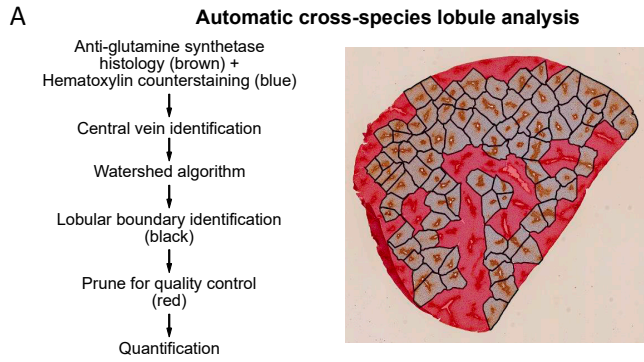
Phylogenetic generalized least squares

Body weight (kg)		
	t-value (correlation)	p-value
Liver weight (kg)	51.38	< 0.0001
Lobule area (mm²)	6.05	< 0.001
Nuclear diameter (µm)	-0.36	0.73
Cell density (mm⁻²)	-1.11	0.28
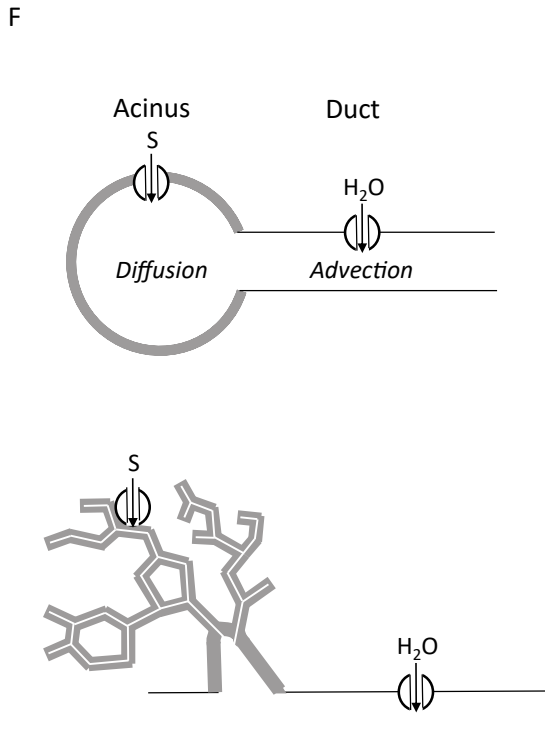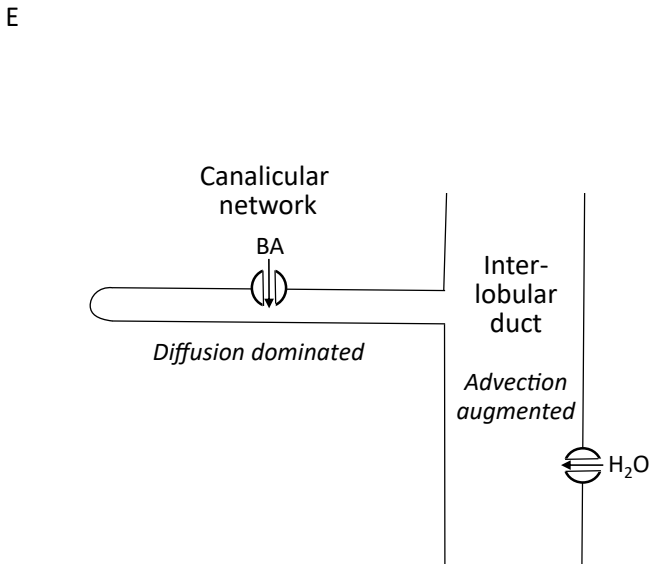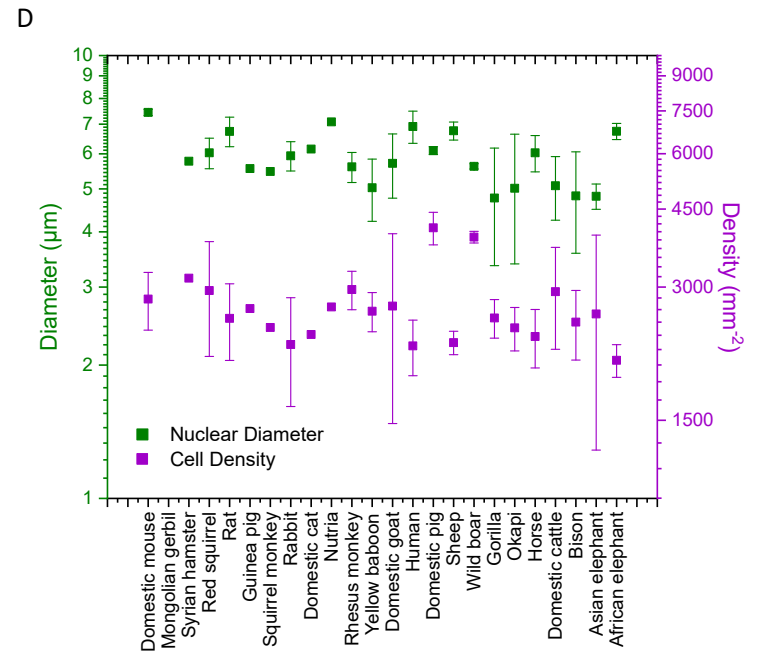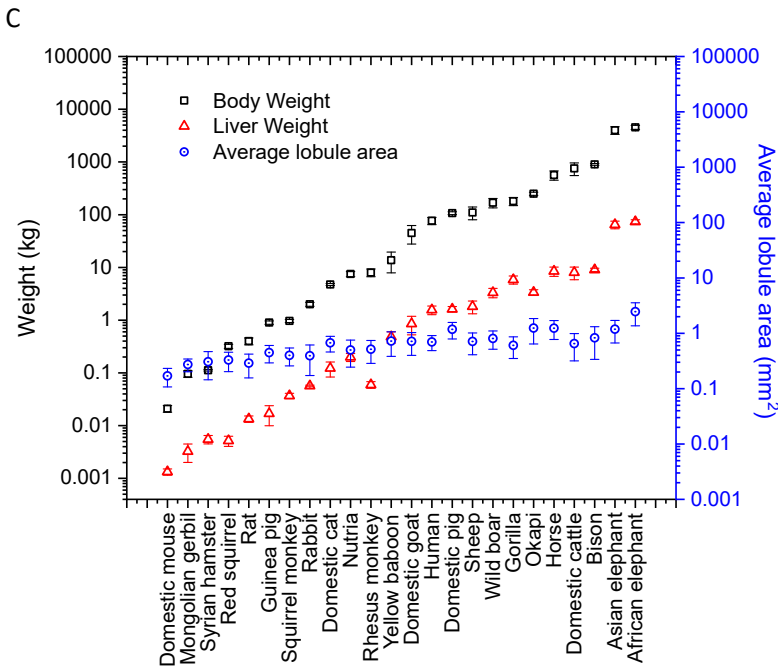
C

Legend:
□ Body Weight
△ Liver Weight
○ Average lobule area

Weight (kg) — Average lobule area (mm²)

D

Legend:
■ Nuclear Diameter
■ Cell Density

Diameter (µm) — Density (mm⁻²)

Species axis: Domestic mouse, Mongolian gerbil, Syrian hamster, Red squirrel, Rat, Guinea pig, Squirrel monkey, Rabbit, Domestic cat, Nutria, Rhesus monkey, Yellow baboon, Domestic goat, Human, Domestic pig, Sheep, Wild boar, Gorilla, Okapi, Horse, Domestic cattle, Bison, Asian elephant, African elephant

E

Canalicular network

BA

Diffusion dominated

Inter-lobular duct

Advection augmented

H_2O

F

Acinus — Duct

S

Diffusion — *Advection*

H_2O

S

H_2O

A. In vivo photoactivation in alternative stripe geometry
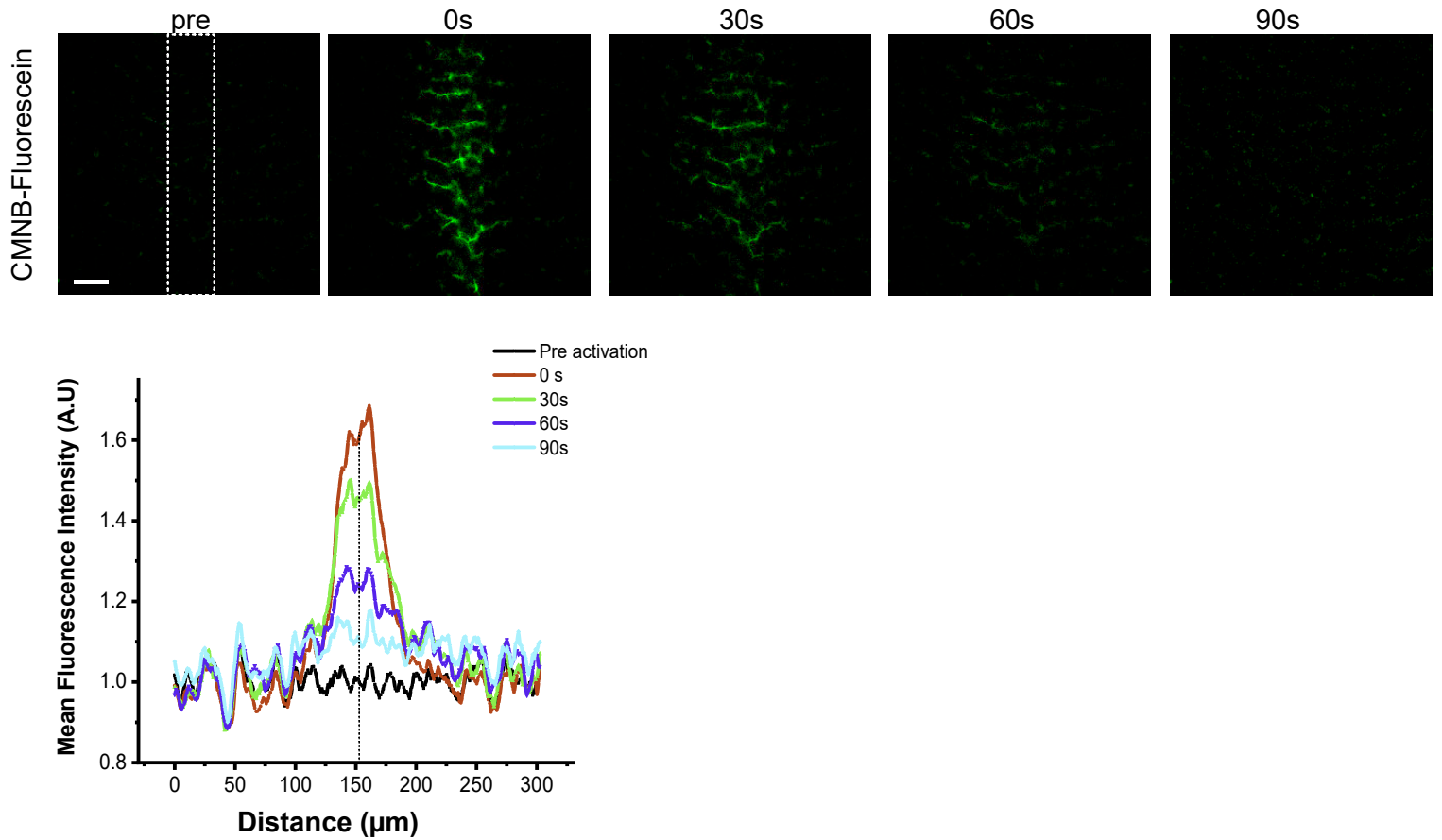
B. In vivo photoactivation (half times)
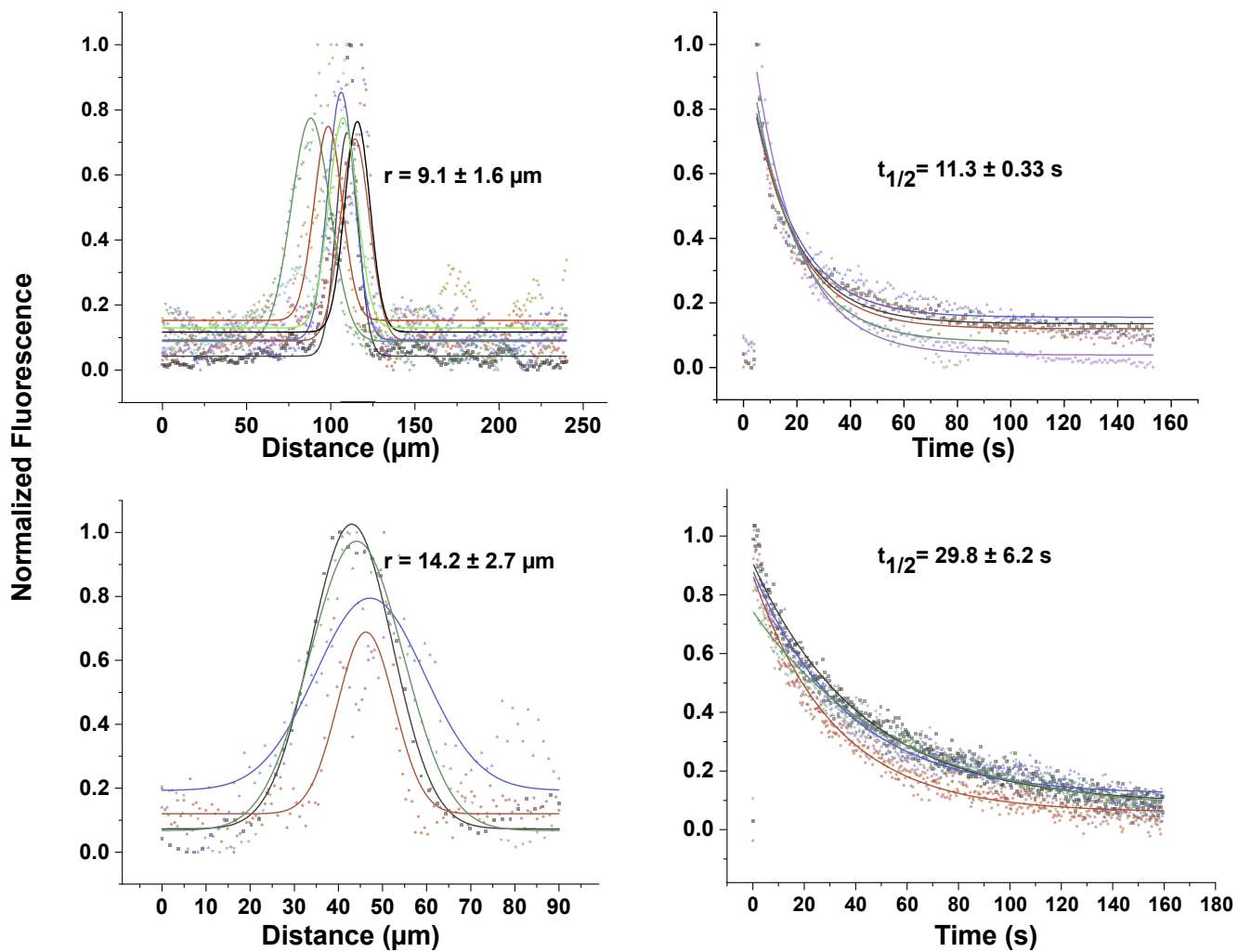
Pre-processing: Removal of artifacts due to immobile structures and aliasing artefacts by Fourier filtering
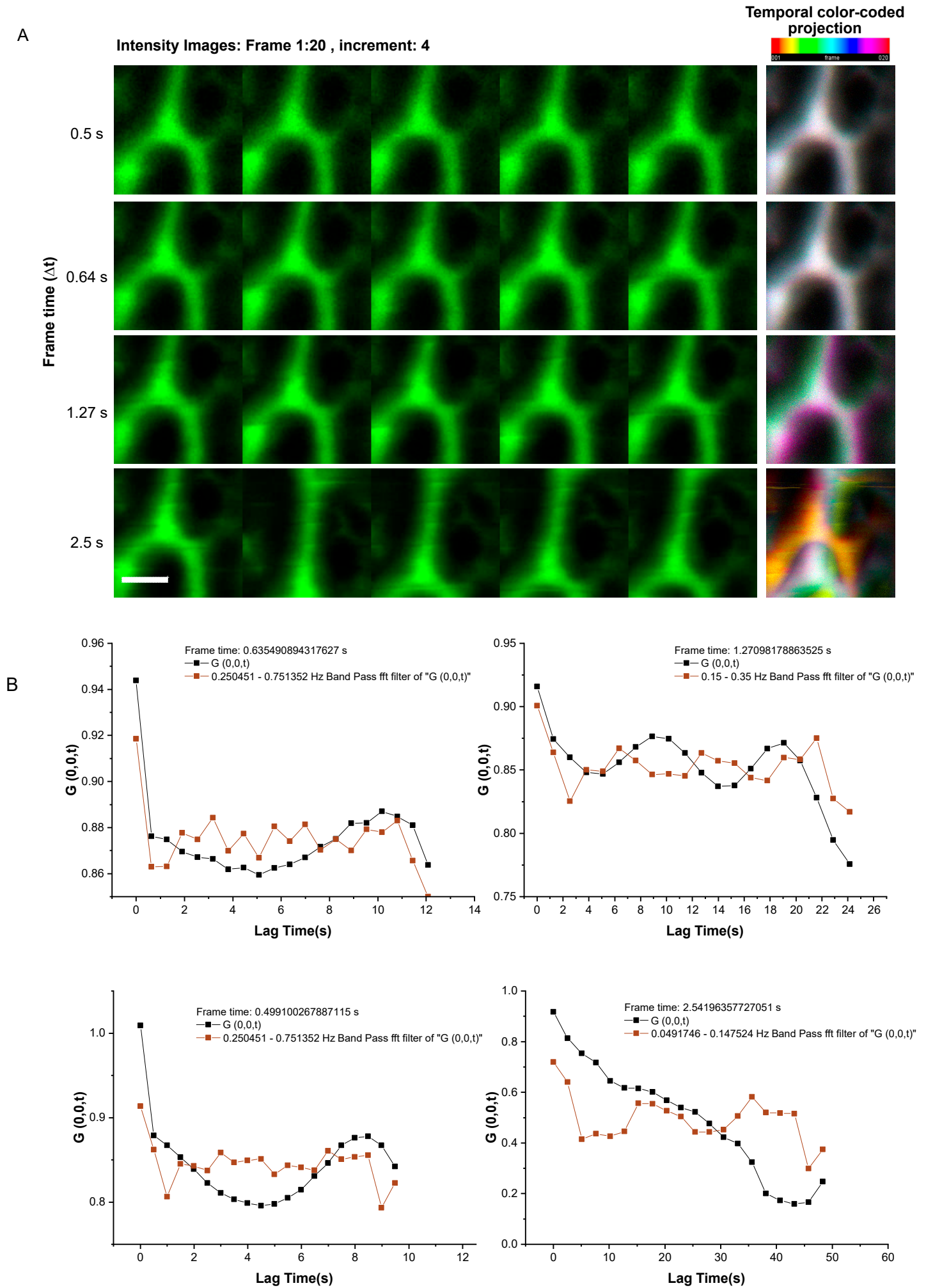
Figure S3

A

Calibration curve: CLF in murine bile

Model	Boltzmann
Equation	y = A2 + (A1-A2)/(1 + exp((x-x0)/dx))
Plot	Mean
A1	-15.52346 ± 4.64193
A2	255.47396 ± 0.23493
x0	173.04988 ± 6.46403
dx	66.99392 ± 3.78895
Reduced Chi-Sqr	2414.36329
R-Square (COD)	0.99942
Adj. R-Square	0.99937
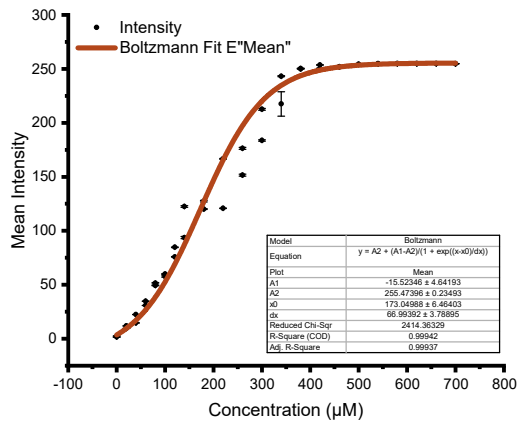
B

In vitro activation of CMNB-Fluorescein in various solvents
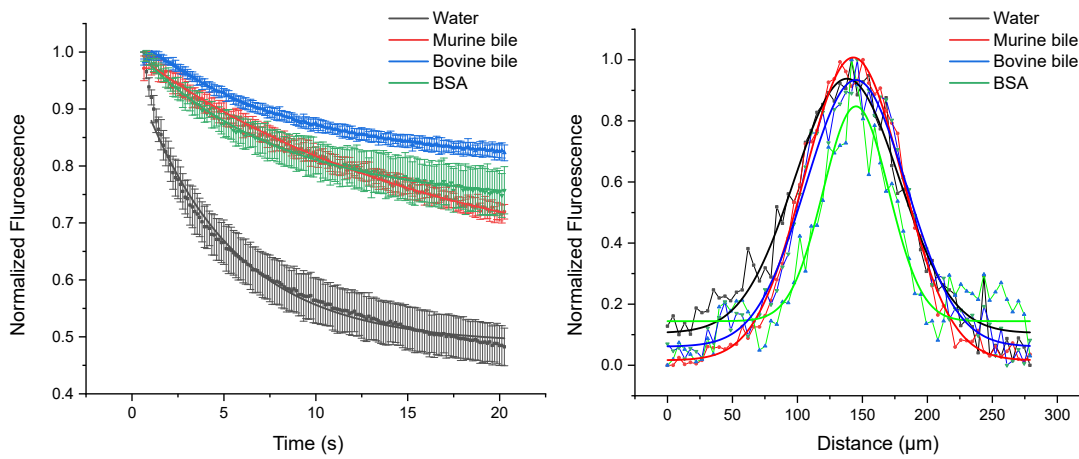
C

Comparison of clearance of alternative fluorophores coupled to cholic acid
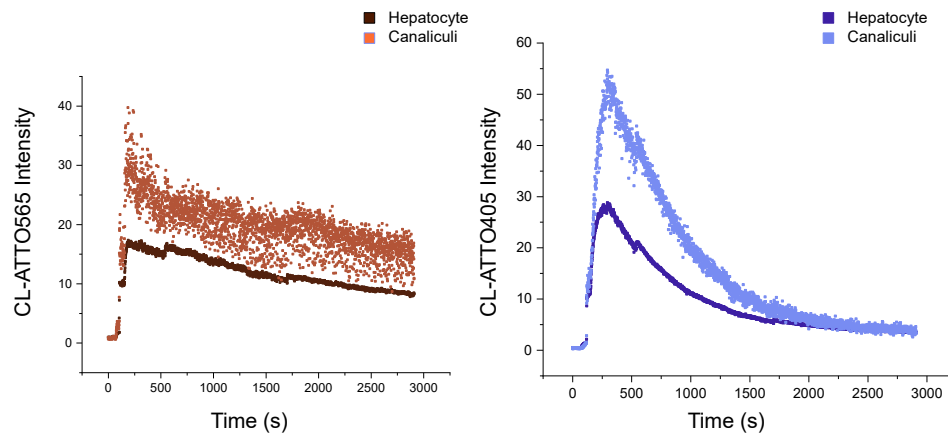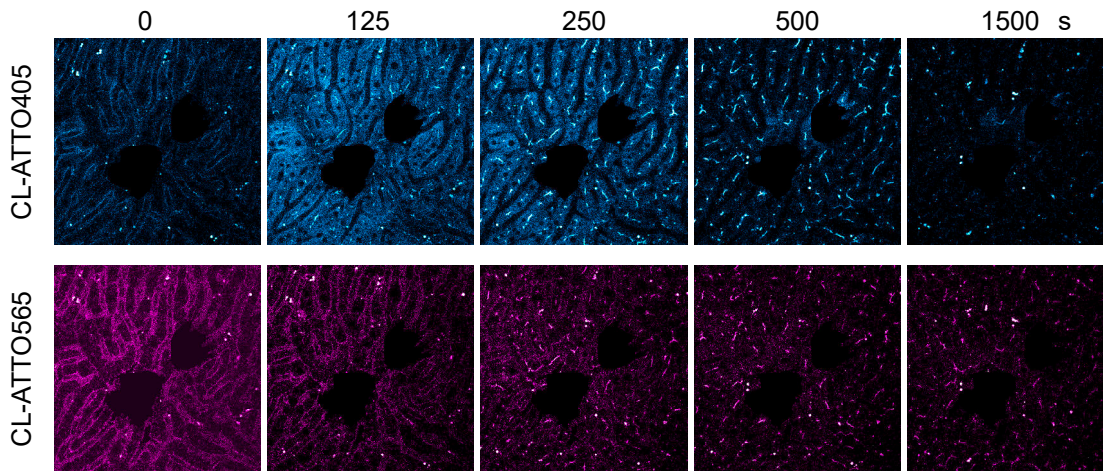
Pearson's Correlation		
	Hepatocyte	
	CL-ATTO405	CL-ATTO656
Canaliculi	0.95	0.85

Figure S4